RIScatter: Unifying Backscatter Communications, Symbiotic Radio, and Reconfigurable Intelligent Surface

Yang Zhao, *Member, IEEE,* and Bruno Clerckx, *Fellow, IEEE*

Abstract—Backscatter Communications (BackCom) switches device load impedance to manipulate the magnitude, phase, and/or frequency responses for information modulation on the scattered carrier. Symbiotic Radio (SR) allows a passive scattering node to ride additional information over the primary radio emitted by an active transmitter, and employs a co-located receiver to decode both sources. Reconfigurable Intelligent Surface (RIS) programs an antenna/metamaterial array to adjust the scattering phase shifts for signal propagation control in specific directions. In this paper, we show how those three seemingly different technologies can be unified to leverage their benefits simultaneously into a single architecture called RIScatter. RIScatter is a new paradigm for future wireless networks and consists of multiple passive scattering nodes, whose reflection states can be adapted to partially engineer the wireless channel and partially modulate information onto the scattered wave. This contrasts with BackCom/SR (resp. RIS) where states are exclusively a function of information symbols (resp. Channel State Information (CSI)). The key principle in RIScatter is to render the probability distribution of reflection states as a joint function of the CSI and input information source, allowing universal hardware design and heterogeneous traffic control. This enables RISscatter to softly bridge, generalize, and outperform BackCom, SR, RIS; boil down to any of those under specific reflection states; or evolve in a mixed setup. We reveal RIScatter provides a fundamental tradeoff that balances information modulation and channel reconfiguration capabilities in a flexible and mutualistic manner. An application scenario is considered where a multi-antenna Access Point (AP) serves a single-antenna user surrounded by multiple RIScatter nodes, and the achievable primary-total-backscatter rate region is characterized by optimizing input distribution at the nodes, active beamforming at the AP, and backscatter decision regions at the user. Simulation results demonstrate RIScatter can exploit the additional propagation paths to provide a smooth transition between backscatter modulation and passive beamforming via smart input distribution design, which includes BackCom, SR, RIS as special cases.

I. Introduction

A. Fundamentals

FUTURE wireless network is envisioned to provide high throughput, uniform coverage, pervasive connectivity, heterogeneous control, and cognitive intelligence for trillions of portable devices. As an emerging low-power communication technique, Backscatter Communications (BackCom) separates conventional transmitter into a Radio-Frequency (RF) carrier emitter with power-hungry elements (e.g., synthesizer and amplifier) and an information-bearing node with power-efficient

The authors are with the Department of Electrical and Electronic Engineering, Imperial College London, London SW7 2AZ, U.K. (e-mail: {yang.zhao18, b.clerckx}@imperial.ac.uk).

components (e.g., harvester and modulator) [1]. The node harvests energy from impinging wave and embeds information over scattered signal in a sustainable and controllable manner. The backscatter reader can be either co-located or separated with the carrier emitter, known as monostatic and bistatic BackCom in Fig. 1(a) and 1(b), respectively. Its applications such as Radio-Frequency Identification (RFID) [2], [3] and passive sensor network [4], [5] have been extensively researched, standardized, and commercialized to support Internet of Things (IoT) and Machine to Machine (M2M) networks. However, traditional BackCom nodes only respond when externally inquired. In Ambient Backscatter Communications (AmBC) [6], interactive nodes recycle ambient signals from legacy transmitters (e.g., radio, television and Wi-Fi) to harvest energy and establish connections. As illustrated in Fig. 1(c), it eliminates the need of dedicated power supply, carrier emitter and frequency spectrum, bringing more opportunities to low-power communications. To combat the strong direct-link interference of AmBC, [7] proposed a co-located receiver that cooperatively decodes both primary (legacy) and backscatter links. The concept of cooperative AmBC was further refined as Symbiotic Radio (SR) in Fig. 1(d) that cognitively incorporates AmBC with existing systems [8]. In SR, the primary transmitter generates active radio and modulates primary information, the passive node scatters incoming wave and superimposes backscatter information, while the co-located receiver decodes both links from both propagation paths. On the other hand, Reconfigurable Intelligent Surface (RIS) in Fig. 1(e) is a promising technology that evolves wireless propagation environment using numerous passive reflecting elements (e.g., scattering antenna or programmable metamaterial) with adjustable amplitudes and/or phases [9]. With proper phase shift design, the scattered components can add constructively/destructively with the direct component for signal enhancement/interference suppression. Compared with scattering nodes of BackCom/SR, RIS elements embed no additional information and use fixed reflection pattern over time, which can be optimized and fed back to the transmitter and receiver during coordination phase.

B. Related Works

Similar to Cognitive Radio (CR), the coexistence of primary and backscatter links in SR can be classified into commensal, parasitic, and competitive relationships, whose instantaneous rates, power schemes, and outage probabilities were acquired in [10], [11]. To evaluate the performance of cooperative SR
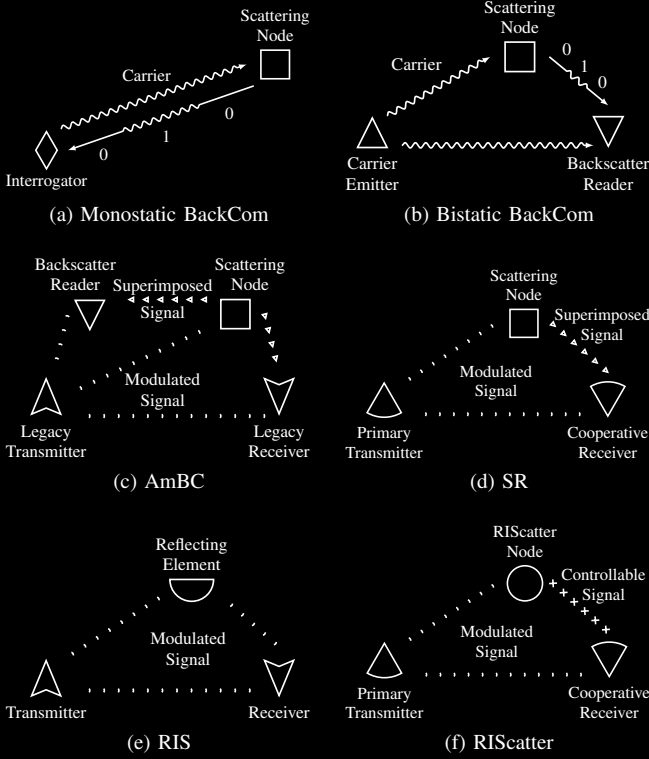
Fig. 1. Paradigms for various scattering applications.

receivers, [7] derived the bit error rates of Maximum-Likelihood (ML), linear, and Successive Interference Cancellation (SIC) detectors for flat fading channels, then proposed a low-complexity detector for frequency-selective fading channels. However, it assumed equal symbol period of both links with perfect synchronization, which is impractical due to the load-switching speed constraint. Although joint ML decoding achieves the optimal detection performance for arbitrary backscatter-over-primary symbol period ratio, the computational complexity is prohibitive especially for high-order constellations [7], [8], [12]. For sequential primary-backscatter decoding, the randomness of backscatter modulation can be modelled as either interference or channel uncertainty, depending on the symbol period ratio [13]. If this ratio is sufficiently large, the authors proved the non-coherent primary achievable rate would approach its coherent counterpart asymptotically. This motivated [7], [8], [10]–[18] to perform SIC from primary to backscatter links. However, the advantages of such SIC remain questionable as 1) primary rate analysis is backed by long backscatter symbol period that constrains backscatter rate; 2) reflection pattern and signal characteristics are not fully exploited; 3) non-coherent primary encoding is required at the transmitter while re-encoding, precoding and subtraction are required at the receiver; 4) primary and backscatter symbols are superimposed by multiplication instead of superposition.

Another open issue for BackCom and SR is node multiple access. [16] proposed a Non-Orthogonal Multiple Access (NOMA)-based SR with SIC order in backscatter equivalent channel strength, whose performance deteriorates fast when the number of nodes increases. Time-Division Multiple Access

(TDMA)-based SR was also considered in [17] where each node transmits information during its dedicated slot and harvests energy during others. It allows adaptive transmission time and reflection ratio optimization, but requires regular feedback and incurs high coordination cost. [19] controls the load-switching speed to shift the scattered signal to the desired frequency band. This enables backscatter Frequency-Division Multiple Access (FDMA) at the cost of extra bandwidth and higher power consumption. To reduce coordination burden for passive nodes, [18] proposed a random code-assisted multiple access for SR and evaluated the asymptotic Signal-to-Interference-plus-Noise Ratio (SINR) using random matrix theory. However, this code-domain solution suffers from imperfect synchronization and the near-far problem.

Conventional RIS design with fixed reflection coefficients during each channel block has been extensively studied in communication, sensing, and power literatures [20]–[25]. In contrast, dynamic RIS that chooses independent reflection coefficients over different time slots has gained recent attentions in multi-user and multi-purpose wireless networks. The concept was first considered for resource blocks of Orthogonal Frequency-Division Multiplexing (OFDM) systems, then extended to power and information phases of Wireless Powered Communication Network (WPCN) [26]–[28]. Dynamic RIS provides artificial channel diversity and flexible resource allocation, but misses the opportunity to encode its own message. From an information-theoretic perspective, [29] reported using RIS as an auxiliary passive beamforming device to maximize the Signal-to-Noise Ratio (SNR) is generally rate-suboptimal for finite input constellations. Instead, joint transmitter-RIS encoding achieves the capacity of RIS-aided channel, and layered encoding with SIC decoding (i.e., SIC-based SR) can outperform pure passive beamforming at high SNR. It inspired [30]–[39] to employ RIS also as an information source to combine passive beamforming and backscatter modulation in the overall reflection pattern. In particular, *symbol level precoding* maps backscatter symbols to optimized RIS coefficient sets [30], [31], *overlay modulation* superposes information-bearing symbols over a common auxiliary matrix [32]–[35], *spatial modulation* switches between reflection coefficient sets that maximize SNR at different receive antennas [36]–[38], and *index modulation* divides RIS into reflection elements for passive beamforming and information elements for on-off modulation [39]. However, those RIS-empowered BackCom/SR designs involve advanced hardware architecture, high optimization complexity, and additional control overhead. Besides, all relevant literatures assumed at backscatter information sources either Gaussian codebook [10], [11], [13]–[17], [34] or finite equiprobable inputs [7], [8], [12], [18], [30]–[33], [35]–[39]. The former is impractical for passive backscatter devices, while the latter does not fully exploit reflection pattern and Channel State Information (CSI).

C. Contributions

We introduce RIScatter that generalizes BackCom, SR, and RIS to manipulate the transmit-assist tradeoff via smart input distribution and practical receiver design. The paradigm of

RIScatter is presented in Fig. 1(f), and the contributions of this paper are summarized as follows.

First, we propose RIScatter nodes to adapt the input probability distribution of a finite-state passive scatter device based on link priority and CSI. The reflection pattern over time is no longer fully random or deterministic, but can be flexibly distributed to unify and balance backscatter modulation with passive beamforming. Scattering source of BackCom/SR and reflecting element of RIS can be regarded as its extreme cases, where the input distribution boils down to equiprobable and degenerate, respectively. Like aforementioned RIS-empowered BackCom/SR schemes, the passive nodes require regular coordination with ambient devices, but the advantages are 1) RIScatter nodes can be built over universal load-switching scatterers instead of composite metamaterial; 2) backscatter modulation and passive beamforming are unified by input distribution instead of advanced hardware architecture; 3) optimization cost of input distribution is much lower than that of RIS reflection coefficients; 4) adaptive backscatter channel coding can exploit CSI to achieve higher instantaneous rate than conventional equiprobable line coding in BackCom/SR; 5) the potentially dispersed characteristics of RIScatter nodes (and legacy users) avoids the development optimization and allows uniformly good performance for both links.

Second, we propose a practical RIScatter receiver that semi-coherently decodes RIScatter nodes from the received energy per backscatter block, re-encodes for their reflection patterns, retrieves primary equivalent channel as if dynamic passive beamforming, then coherently decodes the primary link under the enhanced multipath. The proposed receiver 1) preserves the benefits of backscatter modulation and passive beamforming; 2) enjoys lower computational and operational complexities than joint ML and SIC schemes; 3) accommodates the link difference and suits for diverse symbol period ratios; 4) requires minor modification over legacy hardware.

Third, we consider an application scenario where multiple RIScatter nodes ride over a point-to-point Multiple-Input Single-Output (MISO) transmission, performing backscatter modulation and passive beamforming to a nearby user using shared spectrum, energy, and infrastructures. To investigate how RIScatter unifies BackCom, SR and RIS for the benefits of both coexisting subsystems, we provide primary and backscatter rate analyses and emphasize the contributions of input distribution at RIScatter nodes, active beamforming at the Access Point (AP), and backscatter decision regions at the user. This is the first paper to reveal the importance of those factors in joint RIS and BackCom/SR design.

Fourth, we characterize the achievable primary-total-backscatter rate region of the aforementioned system by optimizing the input distribution, active beamforming, and backscatter decision regions. It is formulated as a weighted sum-rate maximization subject to input probability simplex, average transmit power, and sequential decision threshold constraints. Since the original problem is highly non-convex, we decouple it into individual subproblems and constraint all decision regions to convex (connected) intervals. A suboptimal Block Coordinate Descent (BCD) algorithm is then proposed, where the Karush-Kuhn-Tucker (KKT) input distribution

is numerically evaluated by limit of sequences, the active beamforming is iteratively updated by Projected Gradient Descent (PGD) accelerated by backtracking line search, and the decision regions are refined by existing thresholding designs.

Fifth, we provide numerical results to demonstrate the benefits of RIScatter and proposed algorithms. It is concluded that 1) RIScatter nodes provide flexible transmit-assist tradeoff using adaptive input distribution design; 2) when primary link is absolutely prioritized, the input probability of each node is 1 at one state and 0 at the others, which coincides with discretized RIS; 3) when backscatter link is absolutely prioritized, RIScatter nodes can exploit adaptive channel coding to achieve higher instantaneous rate than conventional equiprobable inputs of BackCom/SR; 4) the proposed KKT input distribution design converges to stationary points, whose average performance is very close to global optimal; 5) the proposed PGD beamforming provides larger rate region than Maximum Ratio Transmission (MRT)-based schemes; 6) the decision region schemes adapted to input distribution provide higher backscatter rates than the non-adaptive ML detector; 7) cooperation between passive nodes in terms of joint encoding can further boost the total backscatter rate; 8) the low complexity of input distribution design and the marginal effect of increasing reflection states motivates the use of low-order scattering nodes to replace high-resolution RIS.

Notations: Italic, bold lower-case, and bold upper-case letters denote scalars, vectors and matrices, respectively. $\mathbf{0}$ and $\mathbf{1}$ denote zero and one array of appropriate size, respectively. $\mathbb{I}^{x \times y}$, $\mathbb{R}_+^{x \times y}$, and $\mathbb{C}^{x \times y}$ denote the unit, real nonnegative, and complex spaces of dimension $x \times y$, respectively. j denotes the imaginary unit. $\mathrm{diag}(\cdot)$ returns a square matrix with the input vector on its main diagonal and zeros elsewhere. $\mathrm{card}(\cdot)$ returns the cardinality of a set. $(\cdot)^*$, $(\cdot)^T$, $(\cdot)^H$, $|\cdot|$, and $\|\cdot\|$ denote the conjugate, transpose, conjugate transpose, absolute value, and Euclidean norm operators, respectively. $(\cdot)^{(r)}$ and $(\cdot)^\star$ denote the r-th iterated and terminal solutions, respectively. The distribution of a Circularly Symmetric Complex Gaussian (CSCG) random variable with zero mean and variance σ^2 is denoted by $\mathcal{CN}(0, \sigma^2)$, and $\sim$ means "distributed as".

II. Scattering Principles

Scattering refers to a change of moving direction of particles after colliding with others. An electromagnetic wave is scattered to many angles when an obstruction is placed in its propagation path. In this section, we first introduce two common scatterer categories and review their operation principles, then briefly discuss how scatterers realize backscatter modulation and channel reconfiguration over reflection patterns.

A. Scatterer Categories

In RF applications such as BackCom, SR and RIS, the scatterer often includes *variable-load antenna* or *programmable metamaterial* with various reflection patterns [40].

1) Antenna-Based Scatterer: A typical antenna-based scatterer consists of an integrated antenna, a load-switching modulator, an energy harvester, and on-chip components (e.g., microcontroller and sensors) [2]. It first receives the impinging

signals, then reradiates some back to the space and dissipates the remainder. According to transmission line theory, the scatter-absorb tradeoff depends on the impedance matching of the load and the antenna. For passive scatterers without dedicated energy source, a majority of incident wave is harvested to support node operation and the reradiated part can be relatively weak [41]. At the receiver, the observed signal can be further decomposed into *structural mode* and *antenna mode* components [42]. The former consistently contributes to environment multipath and is modelled within channel estimation, while the latter depends on impedance mismatch and can be used for backscatter modulation [1] and/or channel reconfiguration [40]. For antenna-based scatterers, the reflection coefficient at load state m is[1]

$$\Gamma_m = \frac{Z_m - Z_A^*}{Z_m + Z_A}, \tag{1}$$

where Z_m is the load impedance at state m and Z_A is the antenna input impedance.

2) Metamaterial-Based Scatterer: A typical metamaterial-based scatterer consists of multiple material layers and a smart controller [43]. The outer metamaterial layer involves numerous sub-wavelength structural units made of metallic or dielectric materials. The properties of unit cells can be artificially tuned for unconventional effective permittivity ϵ and permeability μ, producing customizable response to the electromagnetic field [44]. Using epsilon-negative material (e.g., conducting rods) or mu-negative material (e.g., split-ring resonators), ideal metamaterial-based scatterers can reflect the incident waves at the boundary between free space and metamaterial without receiving them [45]. This mainly applies a phase shift on the reflected wave and any propagation into the metamaterial would be evanescent. Depending on the type of metamaterial, its equivalent impedance can be controlled by voltage (for functional materials [46] and tunable diodes [47]) or architecture (for resonant elements [48]). For metamaterial-based scatterers with a discrete impedance set, the reflection coefficient at metamaterial state m is

$$\Gamma_m = \frac{Z_m - Z_0}{Z_m + Z_0}, \tag{2}$$

where Z_m is the equivalent impedance of metamaterial unit at state m and $Z_0 = 377\Omega$ is the characteristic impedance of free space.

B. BackCom/SR: Backscatter Modulation

BackCom and SR commonly employ antenna-based scatterers as passive information sources. By *frequently switching* between the available states, each scattering node encodes self message over scattered signal and introduces backscatter uncertainty at the receiver. For M-ary Quadrature Amplitude Modulation (QAM), reflection coefficient Γ_m maps to the corresponding *complex constellation point* c_m by

$$\Gamma_m = \alpha \frac{c_m}{\max_{m'}|c_{m'}|}, \tag{3}$$

where $\alpha \in \mathbb{I}$ is the amplitude scattering ratio at the direction of interest.

---

[1]It corresponds to a linear scatter model where the reflection coefficient is irrelevant to incident electromagnetic field strength.

C. RIS: Channel Reconfiguration

RIS typically involves a planar antenna array or metasurface of numerous metamaterial units as a passive channel reconfigurator. By *adaptively choosing* the reflection pattern, each reflecting element alters the phase of scattered signal for constructive/destructive superposition at the receiver. For each unit with M candidate states, reflection coefficient Γ_m maps to the corresponding *phase shift* θ_m by

$$\Gamma_m = \beta_m \exp(j\theta_m), \tag{4}$$

where $\beta_m \in \mathbb{I}$ is the overall amplitude scattering ratio of state m. Lossless RIS assumes $\beta_m = 1$ to maximize the available scattering power.

D. Opportunities

We have seen conventional scattering applications as Back-Com, SR and RIS using the reflection pattern (1), (2) for either backscatter modulation (3) or passive beamforming (4). A natural but critical question is, for a given scatterer with pre-determined reflection pattern set, *can we softly bridge backscatter modulation and passive beamforming by appropriate reflection design?* This question is answered in Section III.

III. RISCATTER

Using shared spectrum, energy and infrastructures, RIScatter is a novel passive communication/assistance protocol that generalizes BackCom, SR and RIS from the perspective of input distribution. In particular, the potentially dispersed passive RIScatter nodes ride over an active legacy transmission in a flexible and mutualistic manner, while the practical RIScatter receiver cooperatively decodes both primary and backscatter links under the benefits of backscatter modulation and passive beamforming.

A. RIScatter Nodes

Based on link priority and CSI, RIScatter nodes adapt the *state input probability distribution* of antenna-based scatterers to unify backscatter modulation and passive beamforming. Conventional line-coded BackCom/SR nodes (e.g., EPC Gen 2 UHF RFID using FM0) and deterministic RIS elements can be viewed as its extreme cases, where the input distribution boils down to equiprobable and degenerate, respectively. As illustrated in Fig. 2, instead of always using fully random or deterministic reflection pattern over time, each RIScatter node can *flexibly adjust* its input distribution to balance information encoding and channel reconfiguration. That is, it semi-randomly select the reflection state per backscatter symbol block under the guidance of input probability $P(\Gamma_m)$ for state m. Such an adaptive backscatter channel coding coincides with RIS when primary link is absolutely prioritized, and outperforms the conventional equiprobable line-coded BackCom/SR when backscatter link is absolutely prioritized. Besides, the dispersed characteristics of RIScatter nodes (and legacy users) avoids the development optimization and allows uniformly good performance for both links.
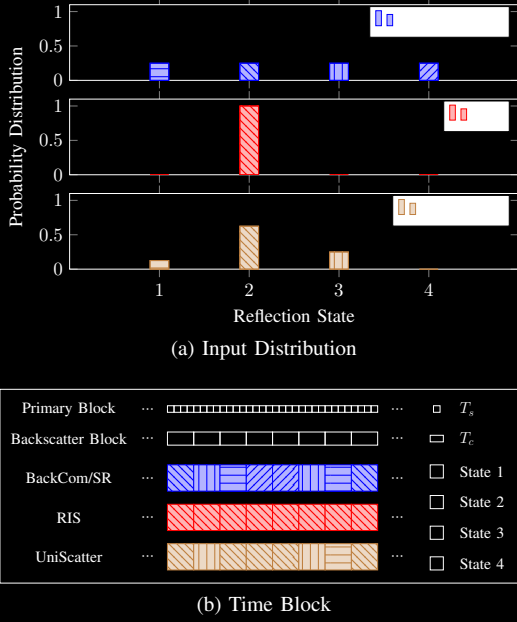
(a) Input Distribution

(b) Time Block

Fig. 2. Input probability distribution and time block structure of BackCom, SR, RIS, and RIScatter. T_s and T_c respectively denote the primary and backscatter symbol period. Within channel coherence time, RIScatter nodes semi-randomly select reflection state for each backscatter symbol block under the guidance of input probability distribution.

As shown in Fig. 3(a), RIScatter nodes can be implemented over readily available passive backscatter devices with energy harvester and information decoder. Its equivalent circuit and scatter model are presented in Fig. 3(b) and 3(c). When activated by primary transmitter, each node harvests a proportion of the impinging wave for its own operation, decode the embedded coordination information for input distribution control, then applies a potentially random phase shift on the reradiated signal due to backscatter modulation. Energy harvesting and information decoding at passive RIScatter nodes can be realized using conventional power-splitting or time-sharing Simultaneous Wireless Information and Power Transfer (SWIPT) protocols [49] or integrated energy-information receiver with pulse position modulated signal [50]. Besides, relevant CSI can be acquired using either traditional sequential methods [51]–[53] or the state-of-the-art parallel approach [54]. In the following context, we assume perfect primary-total-backscatter coordination and perfect channel estimation for all links.

B. RIScatter Receiver

Since each passive RIScatter node directly modulates its own message over the legacy signal, it involves a *double modulation* where the primary and backscatter symbols are superimposed by *multiplication coding* instead of superposition coding. Besides, the backscatter symbol period is typically longer than primary due to the load switching speed constraint. Those facts imply *backscatter detection* under primary uncertainty can be viewed as part of *primary channel training*. Hence, we propose a practical RIScatter receiver that semi-coherently decodes RIScatter nodes from the received energy per backscatter block, re-encodes for their reflection patterns, retrieves primary equivalent channel as if dynamic passive

beamforming, then coherently decodes the primary link under the enhanced multipath. As illustrated in Fig. 4, the total received energy per backscatter block is a random variable that follows different distributions conditioned on different input state hypotheses. Compared with conventional joint ML and SIC from stronger primary link to weaker backscatter links, RIScatter receiver not only preserves the benefits of backscatter modulation and passive beamforming, but also enjoys much lower computational and operational complexities.

C. System Model

To demonstrate the advantages of RIScatter, we consider a single-user multi-node MISO RIScatter system as shown in Fig. 5. In the primary active point-to-point system, a Q-antenna AP transmits to a single-antenna user assisted by K nearby single-antenna RIScatter nodes with M reflection states. In the secondary backscatter Multiple Access Channel (MAC) system, the AP serves as the carrier emitter, the distributed RIScatter nodes modulate information over reradiated RF signals, and the user decodes their messages. For simplicity, we consider a quasi-static block fading model where channels remain constant within coherence block and vary independently between consecutive blocks. Due to the physical constraints of load switching speed, we assume the backscatter over primary symbol period ratio is an integer $N \gg 1$. We also omit the signal reflected by two or more times and ignore the propagation time difference of different paths.

Denote the AP-user direct channel as $\boldsymbol{h}_{\mathrm{D}}^H \in \mathbb{C}^{1 \times Q}$, the AP-node $k \in \mathcal{K} \triangleq \{1,...,K\}$ forward channel as $\boldsymbol{h}_{\mathrm{F},k}^H \in \mathbb{C}^{1 \times Q}$, the node k-user backward channel as $h_{\mathrm{B},k}$, and the cascaded channel via tag k as $\boldsymbol{h}_{\mathrm{C},k}^H \triangleq h_{\mathrm{B},k} \boldsymbol{h}_{\mathrm{F},k}^H \in \mathbb{C}^{1 \times Q}$. Let $x_{\mathcal{K}} \triangleq (x_1, ..., x_K)$ be the backscatter symbol tuple of all RIScatter nodes. Without loss of generality, we consider one specific backscatter block (i.e., N primary blocks) in the following context. Due to double modulation, the primary equivalent channel is a function of *coded* backscatter symbols

$$\boldsymbol{h}_{\mathrm{E}}^H(x_{\mathcal{K}}) \triangleq \boldsymbol{h}_{\mathrm{D}}^H + \sum_{k \in \mathcal{K}} \alpha_k \boldsymbol{h}_{\mathrm{C},k}^H x_k = \boldsymbol{h}_{\mathrm{D}}^H + \boldsymbol{x}^H \mathrm{diag}(\boldsymbol{\alpha}) \boldsymbol{H}_{\mathrm{C}}, \quad (5)$$

where $\alpha_k \in \mathbb{I}$ is the amplitude scattering ratio of RIScatter node k, $x_k \in \mathcal{X} \triangleq \{c_1,...,c_M\}$ is the *coded* backscatter symbol of node k, $\boldsymbol{\alpha} \triangleq [\alpha_1,...,\alpha_K]^T \in \mathbb{I}^K$, $\boldsymbol{x} \triangleq [x_1,...,x_K]^H \in \mathcal{X}^K$, and $\boldsymbol{H}_{\mathrm{C}} \triangleq [\boldsymbol{h}_{\mathrm{C},1},...,\boldsymbol{h}_{\mathrm{C},K}]^H \in \mathbb{C}^{K \times Q}$. The signal received by the user at primary block $n \in \mathcal{N} \triangleq \{1,...,N\}$ is

$$y[n] = \boldsymbol{h}_{\mathrm{E}}^H(x_{\mathcal{K}}) \boldsymbol{w} s[n] + v[n], \quad (6)$$

where $s \sim \mathcal{CN}(0,1)$ is the primary symbol, $v \sim \mathcal{CN}(0,\sigma_v^2)$ is the Additive White Gaussian Noise (AWGN), and $\boldsymbol{w} \in \mathbb{C}^Q$ is the active beamforming vector subject to average transmit power constraint $\|\boldsymbol{w}\|^2 \leq P$. Denote $m_k \in \mathcal{M} \triangleq \{1,...,M\}$ as the reflection state index of node k, and $m_{\mathcal{K}} \triangleq (m_1,...,m_K)$ as the state index tuple of all nodes. Conditioned on backscatter index tuple $m_{\mathcal{K}}$, the received signal (6) follows CSCG distribution $y[n] \sim \mathcal{CN}(0,\sigma_{m_{\mathcal{K}}}^2)$, where

$$\sigma_{m_{\mathcal{K}}}^2 = |\boldsymbol{h}_{\mathrm{E}}^H(x_{m_{\mathcal{K}}}) \boldsymbol{w}|^2 + \sigma_v^2 \quad (7)$$

is the received variance and $x_{m_{\mathcal{K}}}$ is the backscatter symbol tuple associated with $m_{\mathcal{K}}$. For node k, let x_{m_k} be the
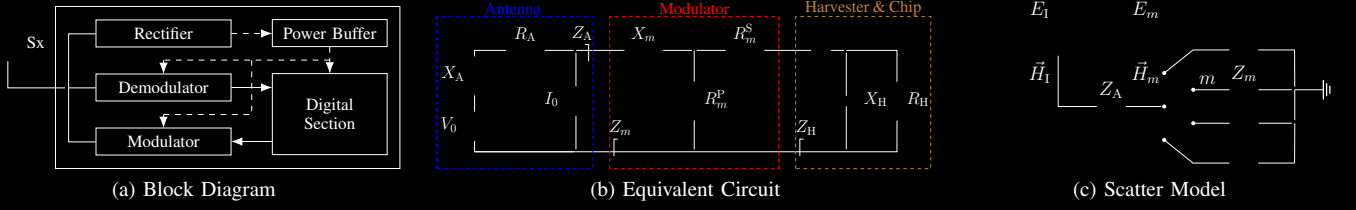
Fig. 3. Block diagram, equivalent circuit, and scatter model of a RIScatter node. The solid and dashed vectors represent signal and energy flows. The scattering antenna behaves as a constant power source, where the voltage V_0 and current I_0 are introduced by incident electric field $\vec{E}_I$ and magnetic field $\vec{H}_I$ [55].
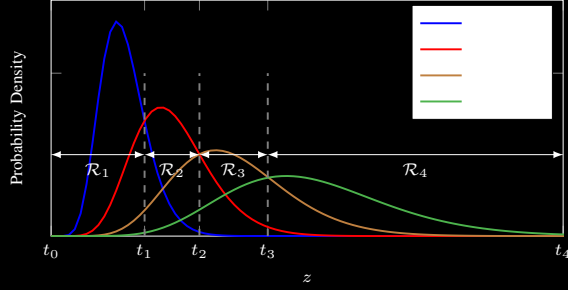

Fig. 4. PDF of total received energy per backscatter block, conditioned on different input state hypotheses. t and $\mathcal{R}$ denote the energy decision thresholds and regions, respectively.

Fig. 5. A single-user multi-node RIScatter system.

backscatter symbol associated with index m_k.[2] Besides, we define the total received energy per backscatter block as $z = \sum_{n=1}^{N} |y[n]|^2$. Since z is the sum of N independent and identically distributed (i.i.d.) exponential variables, its PDF conditioned on $m_{\mathcal{K}}$ follows Gamma distribution

$$f(z|\mathcal{H}_{m_{\mathcal{K}}}) = \frac{z^{N-1} \exp(-z/\sigma_{m_{\mathcal{K}}}^2)}{\sigma_{m_{\mathcal{K}}}^{2N}(N-1)!}, \qquad (8)$$

where $\mathcal{H}_{m_{\mathcal{K}}}$ denotes hypothesis $m_{\mathcal{K}}$. As illustrated in Fig. 4, the RIScatter receiver divides the received energy space into disjoint decision regions associated with those hypotheses. For example, if the total received energy during a backscatter block falls within region $\mathcal{R}_{m_{\mathcal{K}}}$, then the detector output would be $x_{m_{\mathcal{K}}}$.

Remark 1. *Interestingly, the capacity-achieving decision design for Discrete Memoryless Thresholding Channel (DMTC) remains under-investigated, and some attempts were made for a single source with binary inputs [56], [57]. For non-binary inputs with arbitrary distribution, the optimal decision region for each letter can be non-convex (i.e., with*

[2]Please note x_k and $x_{\mathcal{K}}$ are random variable and tuple, while x_{m_k} and $x_{m_{\mathcal{K}}}$ are their instances of index m_k and $m_{\mathcal{K}}$.

non-adjacent partitions) and the optimal number of thresholds is still unknown [58], [59].

Like most existing literatures, we limit the scope of this paper to convex decision regions and consider sequential decision thresholds design therein. For the ease of notations, we define a general bijective function from backscatter index tuple $m_{\mathcal{K}}$ to integer $l \in \mathcal{L} \triangleq \{1,...,L \triangleq M^K\}$, where $\{\sigma_l^2\}_{l \in \mathcal{L}}$ are sorted in an ascending order. Both notations are used interchangeably in the following context. As such, the convex decision region of backscatter tuple l can be written as

$$\mathcal{R}_l \triangleq [t_{l-1}, t_l), \quad 0 \le t_{l-1} \le t_l. \qquad (9)$$

Once the decision threshold vector $\boldsymbol{t} \triangleq [t_0,...,t_L]^T \in \mathbb{R}_+^{(L+1)}$ is determined, we can formulate a Discrete Memoryless Thresholding Multiple Access Channel (DMTMAC) with transition probability from input $x_{m_{\mathcal{K}}}$ to output $\hat{x}_{m'_{\mathcal{K}}}$

$$P(\hat{x}_{m'_{\mathcal{K}}}|x_{m_{\mathcal{K}}}) = \int_{\mathcal{R}_{m'_{\mathcal{K}}}} f(z|\mathcal{H}_{m_{\mathcal{K}}})dz, \qquad (10)$$

then perform backscatter channel coding on top of it.

D. Information Theory

Denote the input probability distribution vector of node k as $\boldsymbol{p}_k \triangleq [P_k(c_1),...,P_k(c_M)]^T \in \mathbb{I}^M$, and the probability of state m_k as $P_k(x_{m_k})$. With independent encoding at all nodes, the probability of backscatter symbol tuple $x_{m_{\mathcal{K}}}$ is

$$P_{\mathcal{K}}(x_{m_{\mathcal{K}}}) = \prod_{k \in \mathcal{K}} P_k(x_{m_k}). \qquad (11)$$

Similar to [60], we define the backscatter information function between input symbol tuple instance $x_{m_{\mathcal{K}}}$ and output symbol tuple variable $\hat{x}_{\mathcal{K}}$ as

$$I_{\mathrm{B}}(x_{m_{\mathcal{K}}}; \hat{x}_{\mathcal{K}}) \triangleq \sum_{m'_{\mathcal{K}}} P(\hat{x}_{m'_{\mathcal{K}}}|x_{m_{\mathcal{K}}}) \log \frac{P(\hat{x}_{m'_{\mathcal{K}}}|x_{m_{\mathcal{K}}})}{P_{\mathcal{K}}(\hat{x}_{m'_{\mathcal{K}}})}, \qquad (12)$$

where $P_{\mathcal{K}}(\hat{x}_{m'_{\mathcal{K}}}) = \sum_{m_{\mathcal{K}}} P_{\mathcal{K}}(x_{m_{\mathcal{K}}})P(\hat{x}_{m'_{\mathcal{K}}}|x_{m_{\mathcal{K}}})$ is the probability of channel output tuple $\hat{x}_{m'_{\mathcal{K}}}$. We also define the backscatter marginal information of letter x_{m_k} of node k as

$$I_{\mathrm{B},k}(x_{m_k}; \hat{x}_{\mathcal{K}}) \triangleq \sum_{m_{\mathcal{K} \setminus \{k\}}} P_{\mathcal{K} \setminus \{k\}}(x_{m_{\mathcal{K} \setminus \{k\}}}) I_{\mathrm{B}}(x_{m_{\mathcal{K}}}; \hat{x}_{\mathcal{K}}), \qquad (13)$$

where $P_{\mathcal{K} \setminus \{k\}}(x_{m_{\mathcal{K} \setminus \{k\}}}) = \prod_{q \in \mathcal{K} \setminus \{k\}} P_q(x_{m_q})$. The backscatter mutual information can be written as

$$I_{\mathrm{B}}(x_{\mathcal{K}}; \hat{x}_{\mathcal{K}}) = \sum_{m_{\mathcal{K}}} P_{\mathcal{K}}(x_{m_{\mathcal{K}}}) I_{\mathrm{B}}(x_{m_{\mathcal{K}}}; \hat{x}_{\mathcal{K}}). \qquad (14)$$

Once backscatter messages of all nodes are successfully decoded, we can re-code for backscatter symbol tuple $x_\mathcal{K}$, recover their reflection patterns by (3), and retrieve the primary equivalent channel by (5). Moreover, we define the primary information function conditioned on backscatter symbol tuple $x_{m_\mathcal{K}}$ as

$$I_\mathrm{P}(s;y|x_{m_\mathcal{K}}) \triangleq \log\Big(1 + \frac{|\boldsymbol{h}_\mathrm{E}^H(x_{m_\mathcal{K}})\boldsymbol{w}|^2}{\sigma_v^2}\Big), \quad (15)$$

the primary marginal information conditioned on letter x_{m_k} of node k as

$$I_{\mathrm{P},k}(s;y|x_{m_k}) \triangleq \sum_{m_{\mathcal{K}\backslash\{k\}}} P_{\mathcal{K}\backslash\{k\}}(x_{m_{\mathcal{K}\backslash\{k\}}})I_\mathrm{P}(s;y|x_{m_\mathcal{K}}), \quad (16)$$

and the primary ergodic mutual information as

$$I_\mathrm{P}(s;y|x_\mathcal{K}) = \sum_{m_\mathcal{K}} P_\mathcal{K}(x_{m_\mathcal{K}})I_\mathrm{P}(s;y|x_{m_\mathcal{K}}). \quad (17)$$

With a slight abuse of notation, we define the corresponding weighted sum information function, marginal information, and mutual information respectively as

$$I(x_{m_\mathcal{K}}) \triangleq \rho I_\mathrm{P}(s;y|x_{m_\mathcal{K}}) + (1-\rho)I_\mathrm{B}(x_{m_\mathcal{K}};\hat{x}_\mathcal{K}), \quad (18)$$
$$I_k(x_{m_k}) \triangleq \rho I_{\mathrm{P},k}(s;y|x_{m_k}) + (1-\rho)I_{\mathrm{B},k}(x_{m_k};\hat{x}_\mathcal{K}), \quad (19)$$
$$I(x_\mathcal{K}) \triangleq \rho I_\mathrm{P}(s;y|x_\mathcal{K}) + (1-\rho)I_\mathrm{B}(x_\mathcal{K};\hat{x}_\mathcal{K}), \quad (20)$$

where $\rho \in \mathbb{I}$ is the relative priority of the primary link.

IV. RATE-REGION CHARACTERIZATION

We notice the primary ergodic mutual information (17) relates to input distribution and active beamforming, while the total backscatter mutual information (14) depends explicitly on input distribution and implicitly on active beamforming and decision thresholds via backscatter DMTMAC (10). To characterize the achievable primary-total-backscatter rate region of the proposed RIScatter system, we aim to maximize the weighted sum mutual information with respect to input distribution $\{\boldsymbol{p}_k\}_{k\in\mathcal{K}}$, active beamforming $\boldsymbol{w}$, and decision thresholds $\boldsymbol{t}$ as

$$\max_{\{\boldsymbol{p}_k\}_{k\in\mathcal{K}},\boldsymbol{w},\boldsymbol{t}} \quad I(x_\mathcal{K}) \quad (21\mathrm{a})$$
$$\text{s.t.} \quad \mathbf{1}^T\boldsymbol{p}_k = 1, \quad \forall k, \quad (21\mathrm{b})$$
$$\boldsymbol{p}_k \geq \mathbf{0}, \quad \forall k, \quad (21\mathrm{c})$$
$$\|\boldsymbol{w}\|^2 \leq P, \quad (21\mathrm{d})$$
$$t_{l-1} \leq t_l, \quad \forall l, \quad (21\mathrm{e})$$
$$\boldsymbol{t} \geq \mathbf{0}. \quad (21\mathrm{f})$$

Problem (21) introduces adaptive backscatter channel coding over conventional BackCom/SR designs. On the other hand, it also generalizes the discrete RIS phase shift selection problem by relaxing the feasible domain from the vertices of M-dimensional probability simplex to the simplex itself. Since problem (21) is highly non-convex, we propose a BCD algorithm that iteratively updates $\{\boldsymbol{p}_k\}_{k\in\mathcal{K}}$, $\boldsymbol{w}$ and $\boldsymbol{t}$ until convergence.

A. Input Distribution

For any given $\boldsymbol{w}$ and $\boldsymbol{t}$, we can construct the equivalent DMTMAC by (10) and simplify (21) to

$$\max_{\{\boldsymbol{p}_k\}_{k\in\mathcal{K}}} \quad I(x_\mathcal{K}) \quad (22\mathrm{a})$$
$$\text{s.t.} \quad (21\mathrm{b}),(21\mathrm{c}), \quad (22\mathrm{b})$$

which involves the coupled term $\prod_{k\in\mathcal{K}} P_k(x_{m_k})$ and is non-convex when $K > 1$. Following [60], we first recast KKT conditions of problem (22) to their equivalent forms, then propose a numerical method that guarantees those conditions on convergence of sequences.

Remark 2. *As demonstrated in [61], KKT conditions are generally necessary but insufficient for total rate maximization problems. Although KKT solutions to problem (22) may end up being saddle points, we will later show by simulation their average performance can be reasonably close to optimal for a moderate K.*

Proposition 1. *The KKT optimality conditions for problem (22) are equivalent to, $\forall k, m_k$,*

$$I_k^\star(x_{m_k}) = I^\star(x_\mathcal{K}), \quad P_k^\star(x_{m_k}) > 0, \quad (23\mathrm{a})$$
$$I_k^\star(x_{m_k}) \leq I^\star(x_\mathcal{K}), \quad P_k^\star(x_{m_k}) = 0. \quad (23\mathrm{b})$$

Proof. Please refer to Appendix A. $\square$

For each node, (23a) suggests each probable state should produce the same marginal information (averaged over all states of other nodes), while (23b) suggests any state with potentially less marginal information should not be used.

Proposition 2. *For any strictly positive initializer $\{\boldsymbol{p}_k^{(0)}\}_{k\in\mathcal{K}}$, the KKT input probability of node k at state m_k is given by the converging point of the sequence*

$$P_k^{(r+1)}(x_{m_k}) = \frac{P_k^{(r)}(x_{m_k})\exp\Big(\frac{\rho}{1-\rho}I_k^{(r)}(x_{m_k})\Big)}{\sum_{m_k'}P_k^{(r)}(x_{m_k'})\exp\Big(\frac{\rho}{1-\rho}I_k^{(r)}(x_{m_k'})\Big)}, \quad (24)$$

where r is the iteration index.

Proof. Please refer to Appendix B. $\square$

For (24) at iteration $r+1$, the input distribution of node k is updated over $\big\{\{\boldsymbol{p}_q^{(r+1)}\}_{q=1}^{k-1}, \{\boldsymbol{p}_q^{(r)}\}_{q=k}^K\big\}$. The KKT input distribution design is summarized in Algorithm 1.

B. Active Beamforming

For any given $\{\boldsymbol{p}_k\}_{k\in\mathcal{K}}$ and $\boldsymbol{t}$, problem (21) reduces to

$$\max_{\boldsymbol{w}} \quad I(x_\mathcal{K}) \quad (25\mathrm{a})$$
$$\text{s.t.} \quad (21\mathrm{d}), \quad (25\mathrm{b})$$

which is still non-convex due to the integration and entropy terms. To tackle this, we rewrite the DMTMAC transition probability (10) from input index tuple $m_\mathcal{K}$ to output index

Algorithm 1: Numerical KKT Input Distribution Evaluation by Limits of Sequence

Input: K, N, $\boldsymbol{h}_{\mathrm{D}}^{H}$, $\boldsymbol{H}_{\mathrm{C}}$, $\boldsymbol{\alpha}$, $\mathcal{X}$, σ_v^2, ρ, $\boldsymbol{w}$, $\boldsymbol{t}$, ϵ
Output: $\{\boldsymbol{p}_k^\star\}_{k\in\mathcal{K}}$

1: Set $\boldsymbol{h}_{\mathrm{E}}^{H}(x_{m_{\mathcal{K}}})$, $\forall m_{\mathcal{K}}$ by (5)
2: $\quad$ $\sigma_{m_{\mathcal{K}}}^2$, $\forall m_{\mathcal{K}}$ by (7)
3: $\quad$ $f(z|\mathcal{H}_{m_{\mathcal{K}}})$, $\forall m_{\mathcal{K}}$ by (8)
4: $\quad$ $P(\hat{x}_{m_{\mathcal{K}}'}|x_{m_{\mathcal{K}}})$, $\forall m_{\mathcal{K}}, m_{\mathcal{K}}'$ by (10)
5: Initialize $r\leftarrow 0$
6: $\quad$ $\boldsymbol{p}_k^{(0)} > \boldsymbol{0}$, $\forall k$
7: Get $P_{\mathcal{K}}^{(r)}(x_{m_{\mathcal{K}}})$, $\forall m_{\mathcal{K}}$ by (11)
8: $\quad$ $I^{(r)}(x_{m_{\mathcal{K}}})$, $\forall m_{\mathcal{K}}$ by (12), (15), (18)
9: $\quad$ $I_k^{(r)}(x_{m_k})$, $\forall k, m_k$ by (13), (16), (19)
10: $\quad$ $I^{(r)}(x_{\mathcal{K}})$ by (14), (17), (20)
11: **Repeat**
12: $\quad$ Update $r\leftarrow r+1$
13: $\quad$ $\boldsymbol{p}_k^{(r)}$, $\forall k$ by (24)
14: $\quad$ Redo step 7–10
15: **Until** $I^{(r)}(x_{\mathcal{K}}) - I^{(r-1)}(x_{\mathcal{K}}) \leq \epsilon$

Algorithm 2: Iterative Active Beamforming Optimization by PGD with Backtracking Line Search

Input: Q, N, $\boldsymbol{h}_{\mathrm{D}}^{H}$, $\boldsymbol{H}_{\mathrm{C}}$, $\boldsymbol{\alpha}$, $\mathcal{X}$, P, σ_v^2, ρ, $\{\boldsymbol{p}_k\}_{k\in\mathcal{K}}$, $\boldsymbol{t}$, α, β, γ, ϵ
Output: $\boldsymbol{w}^\star$

1: Set $\boldsymbol{h}_{\mathrm{E}}^{H}(x_{m_{\mathcal{K}}})$, $\forall m_{\mathcal{K}}$ by (5)
2: $\quad$ $P_{\mathcal{K}}(x_{m_{\mathcal{K}}})$, $\forall m_{\mathcal{K}}$ by (11)
3: Initialize $r\leftarrow 0$
4: $\quad$ $\boldsymbol{w}^{(0)}$, $\|\boldsymbol{w}^{(0)}\|^2 \leq P$
5: Get $(\sigma_{m_{\mathcal{K}}}^{(r)})^2$, $\forall m_{\mathcal{K}}$ by (7)
6: $\quad$ $Q^{(r)}\big(N, \frac{t_{l-1}}{\sigma_{m_{\mathcal{K}}}^2}, \frac{t_l}{\sigma_{m_{\mathcal{K}}}^2}\big)$, $\forall m_{\mathcal{K}}, l$ by (26)
7: $\quad$ $I^{(r)}(x_{\mathcal{K}})$ by (29)
8: $\quad$ $\nabla_{\boldsymbol{w}^*} Q^{(r)}\big(N, \frac{t_{l-1}}{\sigma_{m_{\mathcal{K}}}^2}, \frac{t_l}{\sigma_{m_{\mathcal{K}}}^2}\big)$, $\forall m_{\mathcal{K}}, l$ by (27)
9: $\quad$ $\nabla_{\boldsymbol{w}^*} I^{(r)}(x_{\mathcal{K}})$ by (30)
10: **Repeat**
11: $\quad$ Update $r\leftarrow r+1$
12: $\quad$ $\gamma^{(r)}\leftarrow\gamma$
13: $\quad$ $\bar{\boldsymbol{w}}^{(r)}\leftarrow\boldsymbol{w}^{(r-1)}+\gamma\nabla_{\boldsymbol{w}^*}I^{(r-1)}(x_{\mathcal{K}})$
14: $\quad$ $\boldsymbol{w}^{(r)}$ by (31)
15: $\quad$ Redo step 5–7
16: $\quad$ **While** $I^{(r)}(x_{\mathcal{K}}) < I^{(r-1)}(x_{\mathcal{K}}) + \alpha\gamma\|\nabla_{\boldsymbol{w}^*}I^{(r-1)}(x_{\mathcal{K}})\|^2$
17: $\quad\quad$ Set $\gamma^{(r)}\leftarrow\beta\gamma^{(r)}$
18: $\quad\quad$ Redo step 13–15
19: $\quad$ **End While**
20: $\quad$ Redo step 8, 9
21: **Until** $\|\boldsymbol{w}^{(r)} - \boldsymbol{w}^{(r-1)}\| \leq \epsilon$

l as a regularized incomplete Gamma function in the series representation [62, Theorem 3]

$$Q\Big(N,\frac{t_{l-1}}{\sigma_{m_{\mathcal{K}}}^2},\frac{t_l}{\sigma_{m_{\mathcal{K}}}^2}\Big) = \frac{\int_{t_{l-1}/\sigma_{m_{\mathcal{K}}}^2}^{t_l/\sigma_{m_{\mathcal{K}}}^2} z^{N-1}\exp(-z)dz}{(N-1)!}$$
$$= \exp\Big(-\frac{t_{l-1}}{\sigma_{m_{\mathcal{K}}}^2}\Big)\sum_{n=0}^{N-1}\frac{\big(\frac{t_{l-1}}{\sigma_{m_{\mathcal{K}}}^2}\big)^n}{n!} - \exp\Big(-\frac{t_l}{\sigma_{m_{\mathcal{K}}}^2}\Big)\sum_{n=0}^{N-1}\frac{\big(\frac{t_l}{\sigma_{m_{\mathcal{K}}}^2}\big)^n}{n!}.$$
(26)

Its gradient with respect to $\boldsymbol{w}^*$ can be derived as

$$\nabla_{\boldsymbol{w}^*} Q\Big(N,\frac{t_{l-1}}{\sigma_{m_{\mathcal{K}}}^2},\frac{t_l}{\sigma_{m_{\mathcal{K}}}^2}\Big) = \frac{\boldsymbol{h}_{\mathrm{E}}(x_{m_{\mathcal{K}}})\boldsymbol{h}_{\mathrm{E}}^H(x_{m_{\mathcal{K}}})\boldsymbol{w}}{(\sigma_{m_{\mathcal{K}}}^2)^2} g_{m_{\mathcal{K}}}(t_{l-1}, t_l),$$
(27)

where $g_{m_{\mathcal{K}}}(t_{l-1}, t_l) \triangleq g_{m_{\mathcal{K}}}(t_l) - g_{m_{\mathcal{K}}}(t_{l-1})$ and

$$g_{m_{\mathcal{K}}}(t_l) = t_l\exp\Big(-\frac{t_l}{\sigma_{m_{\mathcal{K}}}^2}\Big)\Big(-1 + \sum_{n=1}^{N-1}\frac{\big(n - \frac{t_l}{\sigma_{m_{\mathcal{K}}}^2}\big)\big(\frac{t_l}{\sigma_{m_{\mathcal{K}}}^2}\big)^{n-1}}{n!}\Big).$$
(28)

On top of (26) and (27), we explicitly express the objective function (25a) and its gradient as (29) and (30) at the end of

page 8, respectively. Those allows problem (25) to be solved by the PGD method, where any unregulated beamforming vector $\bar{\boldsymbol{w}}$ can be projected onto the feasible domain of average transmit power constraint (21d) by

$$\boldsymbol{w} = \sqrt{P}\frac{\bar{\boldsymbol{w}}}{\max\big(\sqrt{P}, \|\bar{\boldsymbol{w}}\|\big)}.$$
(31)

The PGD active beamforming optimization with step size determined by backtracking line search is summarized in Algorithm 2.

$$I(x_{\mathcal{K}}) = \sum_{m_{\mathcal{K}}} P_{\mathcal{K}}(x_{m_{\mathcal{K}}})\Bigg(\rho\log\Big(1 + \frac{|\boldsymbol{h}_{\mathrm{E}}^H(x_{m_{\mathcal{K}}})\boldsymbol{w}|^2}{\sigma_v^2}\Big) + (1-\rho)\sum_{l} Q\Big(N,\frac{t_{l-1}}{\sigma_{m_{\mathcal{K}}}^2},\frac{t_l}{\sigma_{m_{\mathcal{K}}}^2}\Big)\log\frac{Q\Big(N,\frac{t_{l-1}}{\sigma_{m_{\mathcal{K}}}^2},\frac{t_l}{\sigma_{m_{\mathcal{K}}}^2}\Big)}{\sum_{m_{\mathcal{K}}'} P_{\mathcal{K}}(x_{m_{\mathcal{K}}'})Q\Big(N,\frac{t_{l-1}}{\sigma_{m_{\mathcal{K}}'}^2},\frac{t_l}{\sigma_{m_{\mathcal{K}}'}^2}\Big)}\Bigg)$$
(29)

$$\nabla_{\boldsymbol{w}^*} I(x_{\mathcal{K}}) = \sum_{m_{\mathcal{K}}} P_{\mathcal{K}}(x_{m_{\mathcal{K}}})\Bigg(\rho\frac{\boldsymbol{h}_{\mathrm{E}}(x_{m_{\mathcal{K}}})\boldsymbol{h}_{\mathrm{E}}^H(x_{m_{\mathcal{K}}})\boldsymbol{w}}{\sigma_{m_{\mathcal{K}}}^2} + (1-\rho)\sum_{l}\Bigg(\log\frac{Q\Big(N,\frac{t_{l-1}}{\sigma_{m_{\mathcal{K}}}^2},\frac{t_l}{\sigma_{m_{\mathcal{K}}}^2}\Big)}{\sum_{m_{\mathcal{K}}'} P_{\mathcal{K}}(x_{m_{\mathcal{K}}'})Q\Big(N,\frac{t_{l-1}}{\sigma_{m_{\mathcal{K}}'}^2},\frac{t_l}{\sigma_{m_{\mathcal{K}}'}^2}\Big)} + 1\Bigg)$$
$$\times\nabla_{\boldsymbol{w}^*} Q\Big(N,\frac{t_{l-1}}{\sigma_{m_{\mathcal{K}}}^2},\frac{t_l}{\sigma_{m_{\mathcal{K}}}^2}\Big) - \frac{Q\Big(N,\frac{t_{l-1}}{\sigma_{m_{\mathcal{K}}}^2},\frac{t_l}{\sigma_{m_{\mathcal{K}}}^2}\Big)\sum_{m_{\mathcal{K}}'} P_{\mathcal{K}}(x_{m_{\mathcal{K}}'})\nabla_{\boldsymbol{w}^*} Q\Big(N,\frac{t_{l-1}}{\sigma_{m_{\mathcal{K}}'}^2},\frac{t_l}{\sigma_{m_{\mathcal{K}}'}^2}\Big)}{\sum_{m_{\mathcal{K}}'} P_{\mathcal{K}}(x_{m_{\mathcal{K}}'})Q\Big(N,\frac{t_{l-1}}{\sigma_{m_{\mathcal{K}}'}^2},\frac{t_l}{\sigma_{m_{\mathcal{K}}'}^2}\Big)}\Bigg)$$
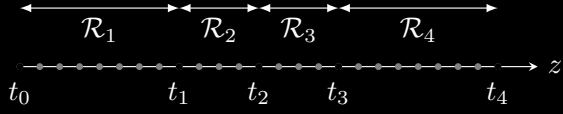(30)

Fig. 6. The decision thresholds are selected from fine-grained discrete energy levels instead of continuous space, and each decision region consists of at least one neighbor energy bins.

C. Decision Threshold

For any given $\{\boldsymbol{p}_k\}_{k\in\mathcal{K}}$ and $\boldsymbol{w}$, problem (21) reduces to

$$\max_{\boldsymbol{t}} \quad I(x_{\mathcal{K}}) \tag{32a}$$

$$\text{s.t.} \quad (21e),(21f), \tag{32b}$$

which is still non-convex because variable $\boldsymbol{t}$ appears on the limits of integration (10). Fortunately, we can further simplify problem (32) as a point-to-point rate-optimal quantizer optimization for a discrete-input continuous-output memoryless channel, thanks to Remark 3 and 4.

Remark 3. *Upon successful backscatter decoding, RIScatter receiver can always re-encode node messages to recover their reflection patterns at each primary block. Therefore, backscatter decision design has no impact on the primary achievable rate, and any thresholding scheme maximizing the total backscatter mutual information (14) is also optimal for problem (32).*

Remark 4. *In terms of total backscatter rate, the potentially dispersed nodes with given input distribution can be viewed as an equivalent source with augmented alphabet of backscatter symbol tuples $\{x_{m_{\mathcal{K}}}\}$. As such, the DMTMAC (10) is essentially a DMTC, and problem (32) reduces to the rate-optimal quantization design for a discrete-input continuous-output memoryless channel.*

Next, we constrain the feasible domain of problem (32) from continuous space $\mathbb{R}_+^{L+1}$ to finite candidate set (i.e., fine-grained discrete energy levels) $\mathcal{T}^{L+1}$. As shown in Fig. 6, by introducing the extra analog-to-digital conversion step, we can group adjacent high-resolution energy bins for backscatter decision regions. Thus, problem (32) is recast as

$$\max_{\boldsymbol{t}\in\mathcal{T}^{L+1}} \quad I_{\mathrm{B}}(x_{\mathcal{K}};\hat{x}_{\mathcal{K}}) \tag{33a}$$

$$\text{s.t.} \quad (21e), \tag{33b}$$

which can be solved by existing rate-optimal sequential quantizer designs for Discrete Memoryless Channel (DMC). To obtain global optimal solution, [63] started from the quadrangle inequality and proposed a Dynamic Programming (DP) method accelerated by the Shor-Moran-Aggarwal-Wilber-Klawe (SMAWK) algorithm with computational complexity $\mathcal{O}\big(L^2(\mathrm{card}(\mathcal{T}) - L)\big)$, while [64] started from the optimality condition for three neighbor thresholds and presented a traverse-then-bisect algorithm with complexity $\mathcal{O}\big(\mathrm{card}(\mathcal{T})L\log(\mathrm{card}(\mathcal{T})L)\big)$. In Section V, both schemes will be compared with the ML thresholding [65]

$$t_l^{\mathrm{ML}} = N\frac{\sigma_{l-1}^2\sigma_l^2}{\sigma_{l-1}^2-\sigma_l^2}\log\frac{\sigma_{l-1}^2}{\sigma_l^2}, \quad l\in\mathcal{L}\backslash\{L\}, \tag{34}$$
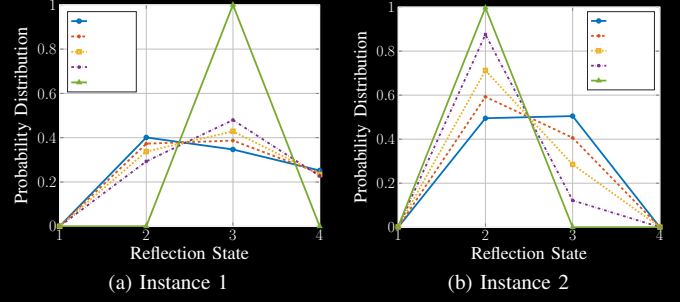

Fig. 7. Typical instances of node input distribution for different weights.

which is generally suboptimal for problem (32) except when all nodes are with equiprobable inputs.

V. SIMULATION RESULTS

In this section, we provide numerical results to evaluate the proposed input distribution, active beamforming, and backscatter decision design for the RIScatter system in Fig. 5. We assume the AP-user distance is $10\,\mathrm{m}$, $K=2$ RIScatter nodes are randomly dropped within a disk of radius $2\,\mathrm{m}$ centered at the user, the AP is with $Q=4$ transmit antennas and an average power budget $P=36\mathrm{dBm}$, the nodes employs 4-QAM with amplitude scattering ratio $\alpha=0.5$, the user is with average noise power $\sigma_v^2=-40\,\mathrm{dBm}$, and the symbol period ratio is $N=20$. For all channels involved, we consider a distance-dependent path loss model

$$L(d)=L_0\left(\frac{d_0}{d}\right)^\gamma \tag{35}$$

together with a Ricean fading model

$$\boldsymbol{H}=\sqrt{\frac{\kappa}{1+\kappa}}\bar{\boldsymbol{H}}+\sqrt{\frac{1}{1+\kappa}}\tilde{\boldsymbol{H}}, \tag{36}$$

where d is the transmission distance, $L_0=-30\mathrm{dB}$ is the reference path loss at distance $d_0=1\mathrm{m}$, κ is the Ricean K-factor, $\bar{\boldsymbol{H}}$ is the deterministic line-of-sight component with entries of unit magnitude, and $\tilde{\boldsymbol{H}}$ is the Rayleigh fading component with entries in standard i.i.d. CSCG distribution. We choose $\gamma_{\mathrm{D}}=2.6$, $\gamma_{\mathrm{F}}=2.4$, $\gamma_{\mathrm{B}}=2$, and $\kappa_{\mathrm{D}}=\kappa_{\mathrm{F}}=\kappa_{\mathrm{B}}=5$ for direct, forward and backward links. The finite threshold domain $\mathcal{T}$ comes from b-bit uniform discretization over the critical interval defined by the confidence bounds of edge hypotheses (i.e., lower bound of $\mathcal{H}_1$ and upper bound of $\mathcal{H}_L$) with confidence level $1-\varepsilon$, where $b=7$ and $\varepsilon=1\times10^{-3}$. All achievable rate curves/regions are averaged over 3000 realizations, and the parameters remain fixed unless otherwise specified.

A. Input Distribution versus Link Priority

The objective of this study is to demonstrate each RIScatter node can adjust its input distribution based on CSI and link priority to balance backscatter modulation and passive beamforming. For this aim, we evaluate the KKT input distribution by Algorithm 1 for a single node under different weights $\rho=\{0,0.1,0.2,0.3,1\}$ in Fig. 7, where 7(a) and 7(b) are two representative instances. We observe that as ρ increases
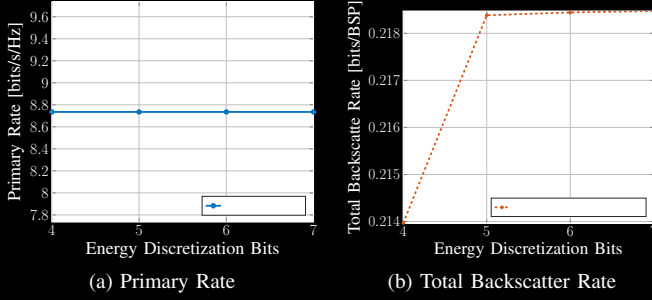
Fig. 8. Average achievable primary and total backscatter rates for different energy discretization bits for $\rho=0$.

from 0 to 1, the KKT input distribution gradually progresses from slightly skewed to completely biased. For $\rho=0$ where backscatter performance is absolutely prioritized, the CSI-adaptive channel coding at the RIScatter node provides higher backscatter rate than conventional BackCom and SR nodes with equiprobable inputs, and some states may end up unused since they cannot produce enough energy difference over the existing alphabet. On the other hand, for $\rho=1$ where primary performance is absolutely prioritized, the input probability is 1 at the state that maximizes the primary equivalent channel strength, and 0 at the others. In this case, the reflection pattern over time is fully deterministic, and the RIScatter node indeed boils down to a RIS element with discrete phase shifts. Those observations meet our s that RIScatter nodes include scattering sources of BackCom/SR and reflecting elements of RIS as special cases, and generalize backscatter modulation and passive beamforming from the perspective of input distribution design. For the BCD algorithm, we choose the KKT input distribution by Algorithm 1, the PGD active beamforming by Algorithm 2, and the SMAWK decision threshold by [63] as reference.

B. Achievable Rates versus Energy Discretization Bits

We now reveal how the analog-to-digital conversion of feasible threshold domain from $\mathbb{R}_+^{L+1}$ to $\mathcal{T}^{L+1}$ affects the average RIScatter performance. For a fixed input distribution and active beamforming, Fig. 8 shows the impact of energy discretization bits b on the average achievable rates when $\rho=0$. We observe the primary rate is a constant for different b as expected from Remark 3. This conclusion holds for arbitrary ρ because the randomness of reflection patterns over time can always be eliminated upon successful backscatter decoding. When the nodes transmit at non-zero total rate, the user can re-encode backscatter messages to recover their reflection patterns at each primary block. Otherwise, the reflection patterns of all nodes are fully deterministic, and the state index tuple can be fed back to the user together with CSI. We also notice increasing b boosts the total backscatter rate and the benefit becomes marginal when b is sufficiently large ($2^b \gg \text{card}(\mathcal{L})$). This is because a larger b allows the decision regions to be constructed from narrower energy bins, which mitigates the transformation loss from problem (32) to (33). Therefore, we conclude a proper selection of b is the key to balance backscatter performance and computational complexity.

(a) Input Distribution

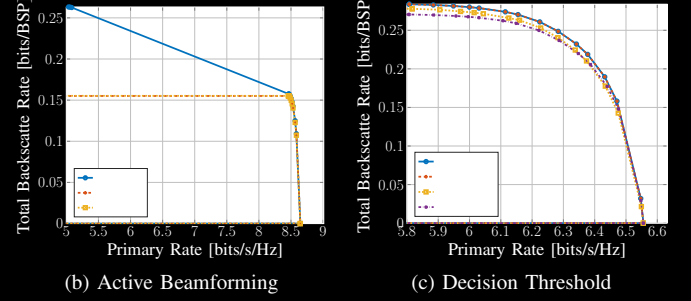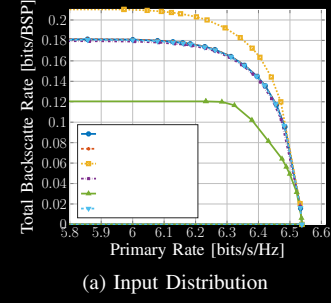(b) Active Beamforming

(c) Decision Threshold

Fig. 9. Average primary-total-backscatter rate regions for different input distribution, active beamforming, and decision threshold schemes. "BSP" means backscatter symbol period.

C. Rate Region by Different Schemes

The average achievable primary-total-backscatter rate regions of various input distribution, active beamforming, and decision threshold schemes are explored in this study.

1) Input Distribution: We compare the following input distribution designs for problem (22):

- *Exhaustion:* Exhaustive grid search over the M-dimensional probability simplex with resolution $\Delta p = 1 \times 10^{-3}$;
- *KKT:* Numerical KKT solution evaluation by Algorithm 1;
- *Cooperation:* Numerical symbol tuple distribution (i.e., K-dimensional joint probability array) evaluation by the Blahut-Arimoto algorithm [66], [67].

Since *Cooperation* involves full transmit cooperation of all nodes, to support independent backscatter encoding, we also propose the following methods to recover individual input distributions from the joint probability array:

- *Marginalization:* Marginal probability distributions;
- *Decomposition:* Normalized rank-1 Canonical Polyadic (CP) decomposition tensors;
- *Randomization:* Random search guided with correlation matrix [68].

Fig. 9(a) shows the achievable rate regions for those input distribution schemes. We observe that *Cooperation* provides the outer bound for all achievable rate regions, which suggests transmit cooperation between RIScatter nodes can be generally helpful. However, it requires joint encoding with arbitrarily dependent codewords, and the extra coordination burden may be unaffordable for a large K. We also notice the average performance of *KKT* input distribution design by Algorithm 1 is extremely close to that of *Exhaustion*, and the loss is indistinguishable for $K=2$. This verifies our claim in Remark 2 that the average performance of KKT solutions can be

reasonably good for a moderate K. Despite *Randomization* yields a similar result, the computational complexity is much higher (loops over $K+1$ linear programming problems) and the performance is backed by numerous randomly generated instances. In contrast, the low-complexity *Marginalization* returns a comparable result and the rate loss is insignificant when K is small. Finally, *Decomposition* suffers from much lower average total backscatter rate, as the rank-1 CP approximation can be inaccurate for some channel-drop realizations. Those observations demonstrate the high performance and low complexity of the proposed KKT input distribution design, and reveal the potential of joint encoding at RIScatter nodes.

2) Active Beamforming: We compare the following active beamforming schemes for problem (25):

- *PGD:* Iterative PGD optimization by Algorithm 2;
- *E-MRT:* MRT towards the ergodic primary equivalent channel $\sum_{m_\mathcal{K}} P_\mathcal{K}(x_{m_\mathcal{K}}) \boldsymbol{h}_\mathrm{E}^H(x_{m_\mathcal{K}})$;
- *D-MRT:* MRT towards the direct channel $\boldsymbol{h}_\mathrm{D}^H$.

Fig. 9(b) plots the achievable rate regions for those active beamforming schemes. In the low-ρ regime, we observe the proposed *PGD* design by Algorithm 2 outperforms *E-MRT* and *D-MRT* in terms of backscatter rate. This is because backscatter decoding relies on the *difference* of received energy expectations under different backscatter symbol tuples. Such an energy diversity is not fully exploited by simply maximizing the direct/ergodic equivalent SNR, but can be properly controlled by *PGD* for enhanced detection performance. As ρ further increases, the primary equivalent SNR outweighs the backscatter energy difference in the weighted sum-rate expression (29), and the input distribution is gradually biased to the state that roughly align direct and scattered components. Therefore, the advantages of distribution-adaptive schemes *PGD* and *E-MRT* become marginal, the ergodic equivalent and direct channels are closer in direction, and the bounds of all schemes approach each other. For the extreme case $\rho=1$, both distribution-adaptive schemes boil down to MRT towards the deterministic primary equivalent channel, as considered in RIS literatures. Those observations prove the proposed *PGD* active beamforming design can balance the primary equivalent SNR and backscatter energy diversity for enlarged rate regions.

3) Decision Threshold: We compare the following decision thresholds for problem (33):

- *DP:* Benchmark DP method for sequential quantizer [63];
- *SMAWK:* DP accelerated by the SMAWK algorithm [63];
- *Bisection:* The traverse-then-bisect algorithm [64];
- *ML:* Maximum likelihood detector (34) [65].

Fig. 9(c) presents the achievable rate region for those decision threshold schemes. We observe that the distribution-adaptive schemes *DP*, *SMAWK* and *Bisection* achieve higher total backscatter rate than the non-adaptive *ML*. This is because the total backscatter mutual information (14) is a function of both input distribution and decision regions, and the rate-optimal threshold design depends heavily on input distribution. For example, the backscatter symbol tuples with zero input probability should never be detected and use empty decision regions, in order to increase the success detection chance of
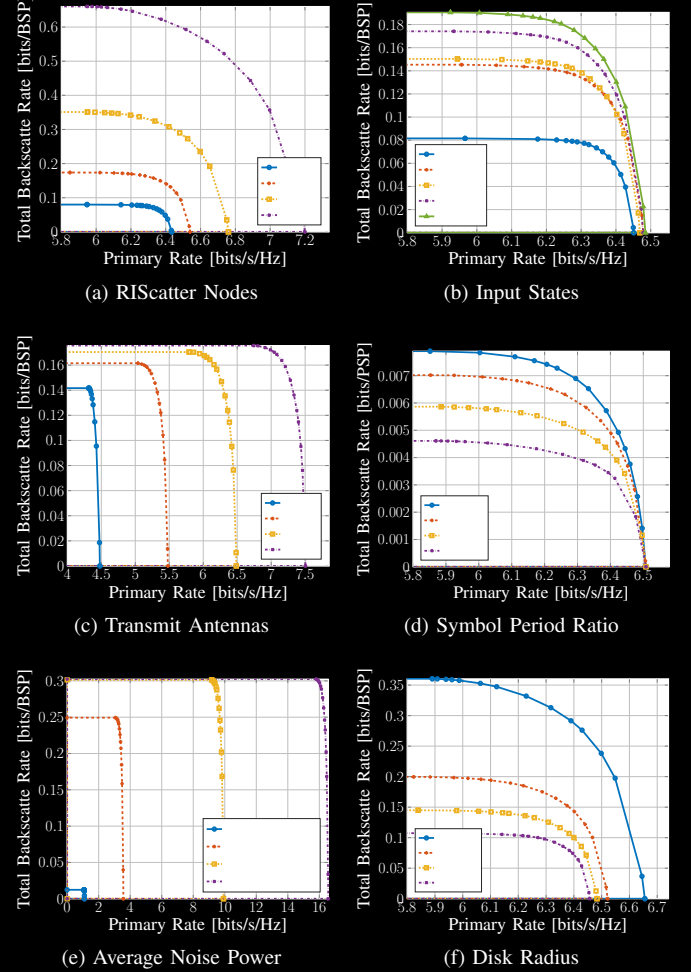

(a) RIScatter Nodes   (b) Input States

(c) Transmit Antennas   (d) Symbol Period Ratio

(e) Average Noise Power   (f) Disk Radius

Fig. 10. Average primary-total-backscatter rate regions for different system configurations. "PSP" means primary symbol period.

other tuples. Those observations highlight the importance of joint input distribution and decision threshold design.

D. Rate Region versus Configuration

In this study, we investigate the impact of system configuration on the average achievable rate regions.

1) Number of Nodes: Fig. 10(a) reveals how the number of two-state RIScatter nodes K influence the primary-backscatter tradeoff. We observe the total backscatter rate roughly scales proportionally with the number of nodes, and the decrease of individual rate is unobvious. This demonstrates the proposed low-complexity semi-coherent energy detector performs reasonably well for a moderate K. On the other hand, we observe adding RIScatter nodes can also boost the achievable primary rate. The reason is the nodes can exploit the additional propagation path for a constructive primary signal superposition that enjoys a "squared law" similar to RIS.

2) Number of States: Fig. 10(b) shows the relationship between available reflection states (i.e., QAM order) M and achievable rate regions. We notice increasing the reflection states has a marginal effect on both primary and total backscatter rates. This is because once the scope is roughly determined,

using denser constellation points may not create enough phase resolution and energy diversity for primary and backscatter links. Another possible reason is the amplitude normalization step in the reflection-constellation mapping (3) grants less scattered (and more harvestable) power for the inner points, which are thus less frequently employed. It motivates the use of numerous elementary RIScatter nodes, instead of high-order transponders or high-resolution metasurfaces.

3) Number of Transmit Antennas: Fig. 10(c) illustrates the impact of transmit antennas Q on the average performance. We observe larger Q produces greater achievable rate regions. Thanks to the PGD active beamforming, the expectations of the received power under different backscatter symbol tuples can be flexibly controlled to satisfy the link priority requirements. For example, beamforming towards the equivalent channel can produce higher primary SNR, while beamforming towards the cascaded channels can enhance the relative energy difference for better backscatter detection. Those observations emphasize the importance of multi-antenna RIScatter systems and demonstrate the advantages of the proposed PGD design.

4) Symbol Period Ratio: Fig. 10(d) presents how symbol period ratio N affects the achievable rate region. We notice using a small N can effectively boost the total backscatter rate per primary symbol, and the conventional SR literatures assuming sufficiently large N is generally inefficient. However, it not only requires a frequent change of reflection states that consumes more power at the passive nodes, but also involves more detection and re-encoding operations at the user to maintain the primary rate. When N becomes sufficiently large, the total backscatter rate approaches 0, and RIScatter nodes boil down to RIS elements with fixed reflection pattern during whole channel block. Therefore, we conclude N should be properly tweaked based on the rate requirements and physical properties of the passive nodes.

5) Average Noise Power: Fig. 10(e) depicts the impact of average noise power σ_v^2 on average rate regions. Despite the proposed low-complexity energy detection is suitable for a wide range of noise levels, there exists a backscatter performance upper bound due to its semi-coherent property. When σ_v^2 relatively high, we can choose a longer backscatter symbol period (i.e., larger N) to maintain the backscatter SNR for better detection performance.

6) Coverage Disk Radius: Fig. 10(f) shows the relationship between RIScatter cover disk radius and achievable rate regions. We observe both primary and backscatter performance are enhanced when nodes are dropped closer to the user. This is because the product path loss (a.k.a. double fading) model for finite-size scatterers is less severe for such near-far setups. Thanks to the dispersed characteristics of RIScatter nodes and legacy users, each node can simply scatter and be decoded by the closest user, thus avoids the development optimization and allows uniformly good performance for both links.

VI. CONCLUSION

This paper introduced RIScatter as a low-power transmit-assist protocol that generalizes BackCom, SR and RIS by smart input distribution and practical receiver design. Starting from scattering principles, we showed how RIScatter nodes include scattering source of BackCom/SR and reflecting element of RIS as special cases, how they can be built over existing passive scatter devices, and how they simultaneously encode self information and assist legacy transmission. We also propose a low-complexity RIScatter receiver that preserves the benefits of backscatter modulation and passive beamforming. The achievable primary-total-backscatter rate region is then studied for a single-user multi-node RIScatter system, where the input distribution, active beamforming, and decision thresholds are iteratively updated. Numerical results not only demonstrated the effectiveness of the proposed algorithms, but also emphasized the importance of adaptive input distribution and cooperative decoding on both primary and backscatter subsystems.

One possible direction is to consider backscatter detection over the received signal domain rather than energy domain. Learning-based classification approaches can be prominsing in such cases. Another interesting question is how to design RIScatter node and receiver in a multi-user system. If one node can be decoded by multiple users, its input distribution may be further adjusted to mimic the multi-beam gain of dynamic passive beamforming [69].

APPENDIX

A. Proof of Proposition 1

Denote the Lagrange multipliers associated with (21b) and (21c) as $\{\nu_k\}_{k\in\mathcal{K}}$ and $\{\lambda_{k,m_k}\}_{k\in\mathcal{K},m_k\in\mathcal{M}}$, respectively. The Lagrangian function of problem (22) is

$$-I(x_\mathcal{K})+\sum_k \nu_k\left(\sum_{m_k} P_k(x_{m_k})-1\right)-\sum_k\sum_{m_k}\lambda_{k,m_k}P_k(x_{m_k})$$
(37)

and the KKT conditions are, $\forall k, m_k,$

$$-\nabla_{P_k^\star(x_{m_k})} I^\star(x_\mathcal{K})+\nu_k^\star-\lambda_{k,m_k}^\star=0, \qquad (38a)$$

$$\lambda_{k,m_k}^\star=0, \quad P_k^\star(x_{m_k})>0, \qquad (38b)$$

$$\lambda_{k,m_k}^\star\geq 0, \quad P_k^\star(x_{m_k})=0, \qquad (38c)$$

where directional derivative is explicitly written as

$$\nabla_{P_k^\star(x_{m_k})} I^\star(x_\mathcal{K})=I_k^\star(x_{m_k})-(1-\rho). \qquad (39)$$

Combining (38) and (39), we have

$$I_k^\star(x_{m_k})=\nu_k^\star+(1-\rho), \quad P_k^\star(x_{m_k})>0, \qquad (40a)$$
$$I_k^\star(x_{m_k})\leq\nu_k^\star+(1-\rho), \quad P_k^\star(x_{m_k})=0, \qquad (40b)$$

such that

$$\sum_{m_k}P_k^\star(x_{m_k})I_k^\star(x_{m_k})=\nu_k^\star+(1-\rho). \qquad (41)$$

On the other hand, by definition (19) we have

$$\sum_{m_k}P_k^\star(x_{m_k})I_k^\star(x_{m_k})=I^\star(x_\mathcal{K}), \qquad (42)$$

where the right-hand side is irrelevant to k. (40), (41), and (42) together complete the proof.

B. Proof of Proposition 2

We first prove sequence (24) is non-decreasing in weighted sum mutual information. Let $P_{\mathcal{K}}(x_{m_{\mathcal{K}}}) = \prod_{q\in\mathcal{K}} P_q(x_{m_q})$ and $P'_{\mathcal{K}}(x_{m_{\mathcal{K}}}) = P'_k(x_{m_k}) \prod_{q\in\mathcal{K}\setminus\{k\}} P_q(x_{m_q})$ be two probability distributions with potentially different marginal for tag k at state m_k, and define an intermediate function $J\big(P_{\mathcal{K}}(x_{m_{\mathcal{K}}}), P'_{\mathcal{K}}(x_{m_{\mathcal{K}}})\big)$ as (43) at the end of page 13. It is straightforward to verify $J\big(P_{\mathcal{K}}(x_{m_{\mathcal{K}}}), P_{\mathcal{K}}(x_{m_{\mathcal{K}}})\big) = I(x_{\mathcal{K}})$ and $J\big(P_{\mathcal{K}}(x_{m_{\mathcal{K}}}), P'_{\mathcal{K}}(x_{m_{\mathcal{K}}})\big)$ is a concave function for a fixed $P'_{\mathcal{K}}(x_{m_{\mathcal{K}}})$. Setting $\nabla_{P^\star_k(x_{m_k})} J\big(P_{\mathcal{K}}(x_{m_{\mathcal{K}}}), P'_{\mathcal{K}}(x_{m_{\mathcal{K}}})\big) = 0$, we have

$$S'_k(x_{m_k}) - S'_k(x_{i_k}) + (1-\rho)\log\frac{P_k(x_{i_k})}{P^\star_k(x_{m_k})} = 0, \quad (44)$$

where $i_k \neq m_k$ is the reference state and

$$S'_k(x_{m_k}) \triangleq I'_k(x_{m_k}) + (1-\rho)\sum_{m_{\mathcal{K}\setminus\{k\}}} P_{\mathcal{K}\setminus\{k\}}(x_{m_{\mathcal{K}\setminus\{k\}}})$$
$$\times \sum_{m'_{\mathcal{K}}} P(\hat{x}_{m'_{\mathcal{K}}}|x_{m_{\mathcal{K}}})\log P'_{\mathcal{K}}(x_{m_{\mathcal{K}}}). \quad (45)$$

Evidently, $\forall m_k \neq i_k$, (44) boils down to

$$P^\star_k(x_{m_k}) = \frac{P'_k(x_{m_k})\exp\left(\frac{\rho}{1-\rho}I'_k(x_{m_k})\right)}{\sum_{m'_k} P'_k(x_{m'_k})\exp\left(\frac{\rho}{1-\rho}I'_k(x_{m'_k})\right)}. \quad (46)$$

Since $P_k(x_{i_k}) = 1 - \sum_{m_k\neq i_k} P^\star_k(x_{m_k})$ has exactly the same form as (46), the choice of reference state i_k does not matter and (46) is indeed optimal $\forall m_k \in \mathcal{M}$. That is, for a fixed $P'_{\mathcal{K}}(x_{m_{\mathcal{K}}})$, choosing $P_k(x_{m_k})$ by (46) ensures

$$J\big(P_{\mathcal{K}}(x_{m_{\mathcal{K}}}), P'_{\mathcal{K}}(x_{m_{\mathcal{K}}})\big) \geq I'(x_{\mathcal{K}}). \quad (47)$$

On the other hand, we also have

$$\Delta \triangleq I(x_{\mathcal{K}}) - J\big(P_{\mathcal{K}}(x_{m_{\mathcal{K}}}), P'_{\mathcal{K}}(x_{m_{\mathcal{K}}})\big) \quad (48a)$$
$$= (1-\rho)\sum_{m_k}\frac{P'_k(x_{m_k})f'_k(x_{m_k})}{\sum_{m'_k} P'_k(x_{m'_k})f'_k(x_{m'_k})}\sum_{m''_{\mathcal{K}}} P(\hat{x}_{m''_{\mathcal{K}}}|x_{m_k})$$
$$\times\log\frac{\sum_{m'_k} P'_k(x_{m'_k})P(\hat{x}_{m''_{\mathcal{K}}}|x_{m'_k})f'_k(x_{m_k})}{\sum_{m'_k} P'_k(x_{m'_k})P(\hat{x}_{m''_{\mathcal{K}}}|x_{m'_k})f'_k(x_{m'_k})} \quad (48b)$$
$$\geq (1-\rho)\sum_{m_k}\frac{P'_k(x_{m_k})f'_k(x_{m_k})}{\sum_{m'_k} P'_k(x_{m'_k})f'_k(x_{m'_k})}\sum_{m''_{\mathcal{K}}} P(\hat{x}_{m''_{\mathcal{K}}}|x_{m_k})$$
$$\times\left(1 - \frac{\sum_{m'_k} P'_k(x_{m'_k})P(\hat{x}_{m''_{\mathcal{K}}}|x_{m'_k})f'_k(x_{m'_k})}{\sum_{m'_k} P'_k(x_{m'_k})P(\hat{x}_{m''_{\mathcal{K}}}|x_{m'_k})f'_k(x_{m_k})}\right) \quad (48c)$$
$$= 0, \quad (48d)$$

where $f'_k(x_{m_k}) \triangleq \exp\left(\frac{\rho}{1-\rho}I'_k(x_{m_k})\right)$ and the equality holds if and only if (46) converges. (47) and (48) together imply $I(x_{\mathcal{K}}) \geq I'(x_{\mathcal{K}})$. Since mutual information is bounded above, we conclude the sequence (24) is non-decreasing and convergent in mutual information.

Next, we prove any converging point of sequence (24), denoted as $P^\star_k(x_{m_k})$, fulfills KKT conditions (23). To see this, let

$$D^{(r)}_k(x_{m_k}) \triangleq \frac{P^{(r+1)}_k(x_{m_k})}{P^{(r)}_k(x_{m_k})} = \frac{f^{(r)}_k(x_{m_k})}{\sum_{m'_k} P^{(r)}_k(x_{m'_k})f^{(r)}_k(x_{m'_k})}. \quad (49)$$

As sequence (24) is convergent, any state with $P^\star_k(x_{m_k}) > 0$ need to satisfy $D^\star_k(x_{m_k}) \triangleq \lim_{r\to\infty} D^{(r)}_k(x_{m_k}) = 1$, namely

$$I^\star_k(x_{m_k}) = \frac{1-\rho}{\rho}\log\sum_{m'_k} P^\star_k(x_{m'_k})f^\star_k(x_{m'_k}), \quad (50)$$

which is reminiscent of (40a) and (23a). That is, given $P^{(0)}_k(x_{m_k}) > 0$, any converging point with $P^\star_k(x_{m_k}) > 0$ must satisfy (23a). On the other hand, we assume $P^\star_k(x_{m_k})$ does not satisfy (23b), such that for any state with $P^\star_k(x_{m_k}) = 0$,

$$I^\star_k(x_{m_k}) > I^\star(x_{\mathcal{K}}) = \sum_{m'_k} P^\star_k(x_{m'_k})I^\star_k(x_{m'_k}), \quad (51)$$

where the equality inherits from (20). Since the exponential function is monotonically increasing, we have $f^\star_k(x_{m_k}) > \sum_{m'_k} P^\star_k(x_{m'_k})f^\star_k(x_{m'_k})$ and $D^\star_k(x_{m_k}) > 1$. Considering $P^{(0)}_k(x_{m_k}) > 0$ and $P^\star_k(x_{m_k}) = 0$, it contradicts with

$$P^{(r)}_k(x_{m_k}) = P^{(0)}_k(x_{m_k})\prod_{n=1}^{r} D^{(n)}_k(x_{m_k}). \quad (52)$$

That is, given $P^{(0)}_k(x_{m_k}) > 0$, any converging point with $P^\star_k(x_{m_k}) = 0$ must satisfy (23b). The proof is thus completed.

REFERENCES

[1] C. Boyer and S. Roy, "Backscatter communication and rfid: Coding, energy, and mimo analysis," *IEEE Transactions on Communications*, vol. 62, pp. 770–785, 3 2014. [Online]. Available: http://ieeexplore.ieee.org/document/6685977/

[2] D. Dobkin, *The RF in RFID: Passive UHF RFID in Practice*. Newnes, 11 2012. [Online]. Available: https://www.elsevier.com/books/the-rf-in-rfid/dobkin/978-0-12-394583-9

[3] J. Landt, "The history of rfid," *IEEE Potentials*, vol. 24, pp. 8–11, 10 2005.

[4] G. Vannucci, A. Bletsas, and D. Leigh, "A software-defined radio system for backscatter sensor networks," *IEEE Transactions on Wireless Communications*, vol. 7, pp. 2170–2179, 6 2008. [Online]. Available: http://ieeexplore.ieee.org/document/4543069/

[5] S. D. Assimonis, S. N. Daskalakis, and A. Bletsas, "Sensitive and efficient rf harvesting supply for batteryless backscatter sensor networks," *IEEE Transactions on Microwave Theory and Techniques*, vol. 64, pp. 1327–1338, 4 2016.

[6] V. Liu, A. Parks, V. Talla, S. Gollakota, D. Wetherall, and J. R. Smith, "Ambient backscatter: Wireless communication out of thin air," *ACM SIGCOMM Computer Communication Review*, vol. 43, pp. 39–50, 9 2013. [Online]. Available: https://dl.acm.org/doi/10.1145/2534169.2486015

[7] G. Yang, Q. Zhang, and Y.-C. Liang, "Cooperative ambient backscatter communications for green internet-of-things," *IEEE Internet of Things Journal*, vol. 5, pp. 1116–1130, 4 2018. [Online]. Available: https://ieeexplore.ieee.org/document/8274950/

[8] Y.-C. Liang, Q. Zhang, E. G. Larsson, and G. Y. Li, "Symbiotic radio: Cognitive backscattering communications for future wireless networks," *IEEE Transactions on Cognitive Communications and Networking*, vol. 6, pp. 1242–1255, 12 2020. [Online]. Available: https://ieeexplore.ieee.org/document/9193946/

$$J\big(P_{\mathcal{K}}(x_{m_{\mathcal{K}}}), P'_{\mathcal{K}}(x_{m_{\mathcal{K}}})\big) \triangleq \sum_{m_{\mathcal{K}}} P_{\mathcal{K}}(x_{m_{\mathcal{K}}})\left(\rho\log\left(1 + \frac{|h^H_E(x_{m_{\mathcal{K}}})w|^2}{\sigma_v^2}\right) + (1-\rho)\sum_{m'_{\mathcal{K}}} P(\hat{x}_{m'_{\mathcal{K}}}|x_{m_{\mathcal{K}}})\log\frac{P(\hat{x}_{m'_{\mathcal{K}}}|x_{m_{\mathcal{K}}})P'_{\mathcal{K}}(x_{m_{\mathcal{K}}})}{P'_{\mathcal{K}}(\hat{x}_{m'_{\mathcal{K}}})P_{\mathcal{K}}(x_{m_{\mathcal{K}}})}\right). \quad (43)$$

[9] Q. Wu, S. Zhang, B. Zheng, C. You, and R. Zhang, "Intelligent reflecting surface-aided wireless communications: A tutorial," *IEEE Transactions on Communications*, vol. 69, pp. 3313–3351, 5 2021. [Online]. Available: https://ieeexplore.ieee.org/document/9326394/

[10] H. Guo, Y.-C. Liang, R. Long, and Q. Zhang, "Cooperative ambient backscatter system: A symbiotic radio paradigm for passive iot," *IEEE Wireless Communications Letters*, vol. 8, pp. 1191–1194, 8 2019. [Online]. Available: https://ieeexplore.ieee.org/document/8692391/

[11] H. Ding, D. B. da Costa, and J. Ge, "Outage analysis for cooperative ambient backscatter systems," *IEEE Wireless Communications Letters*, vol. 9, pp. 601–605, 5 2020. [Online]. Available: https://ieeexplore.ieee.org/document/8941106/

[12] Q. Zhang, Y.-C. Liang, H.-C. Yang, and H. V. Poor, "Mutualistic mechanism in symbiotic radios: When can the primary and secondary transmissions be mutually beneficial?" *IEEE Transactions on Wireless Communications*, vol. 1276, pp. 1–1, 2022. [Online]. Available: https://ieeexplore.ieee.org/document/9751388/

[13] R. Long, Y.-C. Liang, H. Guo, G. Yang, and R. Zhang, "Symbiotic radio: A new communication paradigm for passive internet of things," *IEEE Internet of Things Journal*, vol. 7, pp. 1350–1363, 2 2020. [Online]. Available: https://ieeexplore.ieee.org/document/8907447/

[14] S. Zhou, W. Xu, K. Wang, C. Pan, M.-S. Alouini, and A. Nallanathan, "Ergodic rate analysis of cooperative ambient backscatter communication," *IEEE Wireless Communications Letters*, vol. 8, pp. 1679–1682, 12 2019. [Online]. Available: https://ieeexplore.ieee.org/document/8807353/

[15] T. Wu, M. Jiang, Q. Zhang, Q. Li, and J. Qin, "Beamforming design in multiple-input-multiple-output symbiotic radio backscatter systems," *IEEE Communications Letters*, vol. 25, pp. 1949–1953, 6 2021. [Online]. Available: https://ieeexplore.ieee.org/document/9358202/

[16] J. Xu, Z. Dai, and Y. Zeng, "Enabling full mutualism for symbiotic radio with massive backscatter devices," *arXiv:2106.05789*, 6 2021. [Online]. Available: http://arxiv.org/abs/2106.05789

[17] H. Yang, Y. Ye, K. Liang, and X. Chu, "Energy efficiency maximization for symbiotic radio networks with multiple backscatter devices," *IEEE Open Journal of the Communications Society*, vol. 2, pp. 1431–1444, 2021. [Online]. Available: https://ieeexplore.ieee.org/document/9461158/

[18] S. Han, Y.-C. Liang, and G. Sun, "The design and optimization of random code assisted multi-bd symbiotic radio system," *IEEE Transactions on Wireless Communications*, vol. 20, pp. 5159–5170, 8 2021. [Online]. Available: https://ieeexplore.ieee.org/document/9382925/

[19] G. Vougioukas and A. Bletsas, "Switching frequency techniques for universal ambient backscatter networking," *IEEE Journal on Selected Areas in Communications*, vol. 37, pp. 464–477, 2 2019. [Online]. Available: https://ieeexplore.ieee.org/document/8474355/

[20] Q. Wu and R. Zhang, "Intelligent reflecting surface enhanced wireless network: Joint active and passive beamforming design," vol. 18. IEEE, 12 2018, pp. 1–6. [Online]. Available: https://ieeexplore.ieee.org/document/8647620/

[21] S. Zhang and R. Zhang, "Capacity characterization for intelligent reflecting surface aided mimo communication," *IEEE Journal on Selected Areas in Communications*, vol. 38, pp. 1823–1838, 8 2020. [Online]. Available: https://ieeexplore.ieee.org/document/9110912/

[22] S. Lin, B. Zheng, F. Chen, and R. Zhang, "Intelligent reflecting surface-aided spectrum sensing for cognitive radio," *IEEE Wireless Communications Letters*, vol. 11, pp. 928–932, 5 2022.

[23] Y. Liu, Y. Zhang, X. Zhao, S. Geng, P. Qin, and Z. Zhou, "Dynamic-controlled ris assisted multi-user miso downlink system: Joint beamforming design," *IEEE Transactions on Green Communications and Networking*, vol. 6, pp. 1069–1081, 6 2022.

[24] Z. Feng, B. Clerckx, and Y. Zhao, "Waveform and beamforming design for intelligent reflecting surface aided wireless power transfer: Single-user and multi-user solutions," *IEEE Transactions on Wireless Communications*, 2022.

[25] Y. Zhao, B. Clerckx, and Z. Feng, "Irs-aided swipt: Joint waveform, active and passive beamforming design under nonlinear harvester model," *IEEE Transactions on Communications*, vol. 70, pp. 1345–1359, 2022.

[26] Q. Wu, X. Zhou, and R. Schober, "Irs-assisted wireless powered noma: Do we really need different phase shifts in dl and ul?" *arXiv:2102.08739*, vol. 10, pp. 1493–1497, 7 2021. [Online]. Available: https://ieeexplore.ieee.org/document/9400380/

[27] Q. Wu, X. Zhou, W. Chen, J. Li, and X. Zhang, "Irs-aided wpcns: A new optimization framework for dynamic irs beamforming," *IEEE Transactions on Wireless Communications*, pp. 1–1, 12 2021.

[28] M. Hua and Q. Wu, "Joint dynamic passive beamforming and resource allocation for irs-aided full-duplex wpcn," *IEEE Transactions on Wireless Communications*, pp. 1–1, 12 2021.

[29] R. Karasik, O. Simeone, M. D. Renzo, and S. S. Shitz, "Beyond max-snr: Joint encoding for reconfigurable intelligent surfaces," vol. 2020-June. IEEE, 6 2020, pp. 2965–2970. [Online]. Available: https://ieeexplore.ieee.org/document/9174060/

[30] R. Liu, H. Li, M. Li, and Q. Liu, "Symbol-level precoding design for intelligent reflecting surface assisted multi-user mimo systems." IEEE, 10 2019, pp. 1–6. [Online]. Available: https://ieeexplore.ieee.org/document/8928065/

[31] A. Bereyhi, V. Jamali, R. R. Muller, A. M. Tulino, G. Fischer, and R. Schober, "A single-rf architecture for multiuser massive mimo via reflecting surfaces." IEEE, 5 2020, pp. 8688–8692. [Online]. Available: https://ieeexplore.ieee.org/document/9052989/

[32] X. Xu, Y.-C. Liang, G. Yang, and L. Zhao, "Reconfigurable intelligent surface empowered symbiotic radio over broadcasting signals," vol. 2020-Janua. IEEE, 12 2020, pp. 1–6. [Online]. Available: https://ieeexplore.ieee.org/document/9348236/

[33] Q. Zhang, Y.-C. Liang, and H. V. Poor, "Reconfigurable intelligent surface assisted mimo symbiotic radio networks," *IEEE Transactions on Communications*, vol. 69, pp. 4832–4846, 7 2021. [Online]. Available: https://ieeexplore.ieee.org/document/9391685/

[34] J. Hu, Y. C. Liang, and Y. Pei, "Reconfigurable intelligent surface enhanced multi-user miso symbiotic radio system," *IEEE Transactions on Communications*, vol. 69, pp. 2359–2371, 4 2021.

[35] M. Hua, Q. Wu, L. Yang, R. Schober, and H. V. Poor, "A novel wireless communication paradigm for intelligent reflecting surface based symbiotic radio systems," *IEEE Transactions on Signal Processing*, vol. 70, pp. 550–565, 4 2022. [Online]. Available: http://arxiv.org/abs/2104.09161https://ieeexplore.ieee.org/document/9652042/

[36] E. Basar, "Reconfigurable intelligent surface-based index modulation: A new beyond mimo paradigm for 6g," *IEEE Transactions on Communications*, vol. 68, pp. 3187–3196, 5 2020. [Online]. Available: https://ieeexplore.ieee.org/document/8981888/

[37] T. Ma, Y. Xiao, X. Lei, P. Yang, X. Lei, and O. A. Dobre, "Large intelligent surface assisted wireless communications with spatial modulation and antenna selection," *IEEE Journal on Selected Areas in Communications*, vol. 38, pp. 2562–2574, 11 2020. [Online]. Available: https://ieeexplore.ieee.org/document/9133588/

[38] J. Yuan, M. Wen, Q. Li, E. Basar, G. C. Alexandropoulos, and G. Chen, "Receive quadrature reflecting modulation for ris-empowered wireless communications," *IEEE Transactions on Vehicular Technology*, vol. 70, pp. 5121–5125, 5 2021. [Online]. Available: https://ieeexplore.ieee.org/document/9405433/

[39] S. Hu, C. Liu, Z. Wei, Y. Cai, D. W. K. Ng, and J. Yuan, "Beamforming design for intelligent reflecting surface-enhanced symbiotic radio systems," *arxiv:2110.10316*, 10 2021. [Online]. Available: http://arxiv.org/abs/2110.10316

[40] Y. C. Liang, Q. Zhang, J. Wang, R. Long, H. Zhou, and G. Yang, "Backscatter communication assisted by reconfigurable intelligent surfaces," *Proceedings of the IEEE*, 2022.

[41] S. J. Thomas, E. Wheeler, J. Teizer, and M. S. Reynolds, "Quadrature amplitude modulated backscatter in passive and semipassive uhf rfid systems," *IEEE Transactions on Microwave Theory and Techniques*, vol. 60, pp. 1175–1182, 4 2012. [Online]. Available: http://ieeexplore.ieee.org/document/6153042/

[42] R. Hansen, "Relationships between antennas as scatterers and as radiators," *Proceedings of the IEEE*, vol. 77, pp. 659–662, 5 1989. [Online]. Available: http://ieeexplore.ieee.org/document/32056/

[43] Q. Wu and R. Zhang, "Towards smart and reconfigurable environment: Intelligent reflecting surface aided wireless network," *IEEE Communications Magazine*, vol. 58, pp. 106–112, 1 2020. [Online]. Available: https://ieeexplore.ieee.org/document/8910627/

[44] J. Zhou, P. Zhang, J. Han, L. Li, and Y. Huang, "Metamaterials and metasurfaces for wireless power transfer and energy harvesting," *Proceedings of the IEEE*, vol. 110, pp. 31–55, 1 2022.

[45] Y. Huang, *Antennas: From Theory to Practice.* Wiley, 9 2021.

[46] A. Singh, M. Andrello, N. Thawdar, and J. M. Jornet, "Design and operation of a graphene-based plasmonic nano-antenna array for communication in the terahertz band," *IEEE Journal on Selected Areas in Communications*, vol. 38, pp. 2104–2117, 9 2020.

[47] F. Costa and M. Borgese, "Electromagnetic model of reflective intelligent surfaces," *IEEE Open Journal of the Communications Society*, vol. 2, pp. 1577–1589, 2021.

[48] M. E. Bialkowski and K. H. Sayidmarie, "Investigations into phase characteristics of a single-layer reflectarray employing patch or ring elements of variable size," *IEEE Transactions on Antennas and Propagation*, vol. 56, pp. 3366–3372, 2008.

[49] B. Clerckx, R. Zhang, R. Schober, D. W. K. Ng, D. I. Kim, and H. V. Poor, "Fundamentals of wireless information and power transfer: From rf energy harvester models to signal and system designs," *IEEE Journal on Selected Areas in Communications*, vol. 37, pp. 4–33, 1 2019. [Online]. Available: https://ieeexplore.ieee.org/document/8476597/

[50] J. Kim and B. Clerckx, "Wireless information and power transfer for iot: Pulse position modulation, integrated receiver, and experimental validation," *arXiv:2104.08404*, pp. 1–15, 4 2021. [Online]. Available: http://arxiv.org/abs/2104.08404

[51] D. Bharadia, K. R. Joshi, M. Kotaru, and S. Katti, "Backfi: High throughput wifi backscatter," vol. 45. ACM, 8 2015, pp. 283–296. [Online]. Available: https://dl.acm.org/doi/10.1145/2785956.2787490

[52] G. Yang, C. K. Ho, and Y. L. Guan, "Multi-antenna wireless energy transfer for backscatter communication systems," *IEEE Journal on Selected Areas in Communications*, vol. 33, pp. 2974–2987, 12 2015. [Online]. Available: http://ieeexplore.ieee.org/document/7274644/

[53] H. Guo, Q. Zhang, S. Xiao, and Y.-C. Liang, "Exploiting multiple antennas for cognitive ambient backscatter communication," *IEEE Internet of Things Journal*, vol. 6, pp. 765–775, 2 2019. [Online]. Available: https://ieeexplore.ieee.org/document/8411483/

[54] M. Jin, Y. He, C. Jiang, and Y. Liu, "Parallel backscatter: Channel estimation and beyond," *IEEE/ACM Transactions on Networking*, vol. 29, pp. 1128–1140, 6 2021. [Online]. Available: https://ieeexplore.ieee.org/document/9377568/

[55] Y. Huang, A. Alieldin, and C. Song, "Equivalent circuits and analysis of a generalized antenna system," *IEEE Antennas and Propagation Magazine*, vol. 63, pp. 53–62, 4 2021. [Online]. Available: https://ieeexplore.ieee.org/document/9392844/

[56] J. Qian, Y. Zhu, C. He, F. Gao, and S. Jin, "Achievable rate and capacity analysis for ambient backscatter communications," *IEEE Transactions on Communications*, vol. 67, pp. 6299–6310, 9 2019. [Online]. Available: https://ieeexplore.ieee.org/document/8721108/

[57] T. Nguyen and T. Nguyen, "Capacity achieving quantizer design for binary channels," *IEEE Communications Letters*, vol. 25, pp. 759–763, 3 2021. [Online]. Available: https://ieeexplore.ieee.org/document/9247251/

[58] T. Nguyen, Y.-J. Chu, and T. Nguyen, "On the capacities of discrete memoryless thresholding channels," vol. 2018-June. IEEE, 6 2018, pp. 1–5. [Online]. Available: https://ieeexplore.ieee.org/document/8417506/

[59] T. Nguyen and T. Nguyen, "Optimal quantizer structure for maximizing mutual information under constraints," *IEEE Transactions on Communications*, vol. 69, pp. 7406–7413, 11 2021. [Online]. Available: https://ieeexplore.ieee.org/document/9530430/

[60] M. Rezaeian and A. Grant, "Computation of total capacity for discrete memoryless multiple-access channels," *IEEE Transactions on Information Theory*, vol. 50, pp. 2779–2784, 11 2004. [Online]. Available: http://ieeexplore.ieee.org/document/1347364/

[61] J. Buhler and G. Wunder, "A note on capacity computation for the discrete multiple access channel," *IEEE Transactions on Information Theory*, vol. 57, pp. 1906–1910, 4 2011. [Online]. Available: https://ieeexplore.ieee.org/document/5730559/

[62] G. J. O. Jameson, "The incomplete gamma functions," *The Mathematical Gazette*, vol. 100, pp. 298–306, 7 2016. [Online]. Available: https://www.cambridge.org/core/product/identifier/S002555721600067X/type/journal_article

[63] X. He, K. Cai, W. Song, and Z. Mei, "Dynamic programming for sequential deterministic quantization of discrete memoryless channels," *IEEE Transactions on Communications*, vol. 69, pp. 3638–3651, 6 2021. [Online]. Available: https://ieeexplore.ieee.org/document/9366549/

[64] T. Nguyen and T. Nguyen, "On thresholding quantizer design for mutual information maximization: Optimal structures and algorithms," vol. 2020-May. IEEE, 5 2020, pp. 1–5. [Online]. Available: https://ieeexplore.ieee.org/document/9128966/

[65] J. Qian, A. N. Parks, J. R. Smith, F. Gao, and S. Jin, "Iot communications with m-psk modulated ambient backscatter: Algorithm, analysis, and implementation," *IEEE Internet of Things Journal*, vol. 6, pp. 844–855, 2 2019. [Online]. Available: https://ieeexplore.ieee.org/document/8423609/

[66] S. Arimoto, "An algorithm for computing the capacity of arbitrary discrete memoryless channels," *IEEE Transactions on Information Theory*, vol. 18, pp. 14–20, 1 1972. [Online]. Available: http://ieeexplore.ieee.org/document/1054753/

[67] R. E. Blahut, "Computation of channel capacity and rate-distortion functions," *IEEE Transactions on Information Theory*, vol. 18, pp. 460–473, 7 1972. [Online]. Available: http://ieeexplore.ieee.org/document/1054855/

[68] E. Calvo, D. P. Palomar, J. R. Fonollosa, and J. Vidal, "On the computation of the capacity region of the discrete mac," *IEEE Transactions on Communications*, vol. 58, pp. 3512–3525, 12 2010. [Online]. Available: http://ieeexplore.ieee.org/document/5590317/

[69] C. Qiu, Q. Wu, M. Hua, X. guan, and Y. Wu, "Achieving multi-beam gain in intelligent reflecting surface assisted wireless energy transfer," *arXiv:2205.08893*, 5 2022. [Online]. Available: http://arxiv.org/abs/2205.08893